THE INFRARED LUMINOSITY FUNCTION OF GALAXIES AT REDSHIFTS $z = 1$ AND $z \sim 2$ IN THE GOODS FIELDS

K. I. CAPUTI,[1,2] G. LAGACHE,[1] LIN YAN,[3] H. DOLE,[1] N. BAVOUZET,[1] E. LE FLOC'H,[4]
P. I. CHOI,[3] G. HELOU,[3] AND N. REDDY[5]

ABSTRACT

We present the rest-frame 8 μm LF at redshifts $z = 1$ and ~ 2, computed from *Spitzer* 24 μm–selected galaxies in the GOODS fields over an area of 291 arcmin^2. Using classification criteria based on X-ray data and IRAC colors, we identify the AGNs in our sample. The rest-frame 8 μm LFs for star-forming galaxies at redshifts $z = 1$ and ~ 2 have the same shape as at $z \sim 0$, but with a strong positive luminosity evolution. The number density of star-forming galaxies with $\log_{10}(\nu L_\nu^{8 \, \mu m}) > 11$ increases by a factor >250 from redshift $z \sim 0$ to 1 and is basically the same at $z = 1$ and ~ 2. The resulting rest-frame 8 μm luminosity densities associated with star formation at $z = 1$ and ~ 2 are more than 4 and 2 times larger than at $z \sim 0$, respectively. We also compute the total rest-frame 8 μm LF for star-forming galaxies and AGNs at $z \sim 2$ and show that AGNs dominate its bright end, which is well described by a power law. Using a new calibration based on *Spitzer* star-forming galaxies at $0 < z < 0.6$ and validated at higher redshifts through stacking analysis, we compute the bolometric IR LF for star-forming galaxies at $z = 1$ and ~ 2. We find that the respective bolometric IR luminosity densities are $(1.2 \pm 0.2) \times 10^9$ and $(6.6^{+1.2}_{-1.0}) \times 10^8$ $L_\odot$ Mpc^{-3}, in agreement with previous studies within the error bars. At $z \sim 2$, around 90% of the IR luminosity density associated with star formation is produced by luminous and ultraluminous IR galaxies, with the two populations contributing in roughly similar amounts. Finally, we discuss the consistency of our findings with other existing observational results on galaxy evolution.

Subject headings: galaxies: evolution — galaxies: high-redshift — galaxies: luminosity function, mass function — infrared: galaxies

Online material: color figure

1. INTRODUCTION

Since the *Spitzer Space Telescope* (Werner et al. 2004) became operational in 2003 December, very important progress has been made in understanding the nature and properties of infrared (IR) galaxies. This progress has been revolutionary, in particular, for the study of galaxies at high redshifts ($z > 1$), to which all of the previous IR facilities operating in the wavelength range $\lambda \sim 5$–200 μm had basically no access. Previous missions such as the *Infrared Astronomical Satellite* (*IRAS*) and the *Infrared Space Observatory* (*ISO*) allowed for multiple studies of mid- and far-IR galaxies, but they were restricted to lower redshifts ($z \lesssim 1$) due to their sensitivity limits. Until the launch of *Spitzer*, our vision of the high-redshift IR universe was biased to the relatively small number of galaxies detected in submillimeter and millimeter surveys (e.g., Scott et al. 2002; Webb et al. 2003; Greve et al. 2004).

The sensitivity achieved by the Multiband Imaging Photometer for *Spitzer* (MIPS; Rieke et al. 2004) at 24 μm is enabling us for the first time to conduct systematic studies of IR galaxies at high redshifts. Several recent works have shown that, in contrast to what happens in the local universe, the IR extragalactic light is increasingly dominated by luminous and ultraluminous IR galaxies (LIRGs and ULIRGs, respectively) with increasing redshift (e.g.,

Le Floc'h et al. 2004, 2005; Lonsdale et al. 2004; Yan et al. 2004; Caputi et al. 2006a, 2006c). These LIRGs and ULIRGs constitute an important fraction of the most massive galaxies present at $z \gtrsim 1$ (Caputi et al. 2006a).

In a minor but nonnegligible fraction of high-redshift IR galaxies, the IR emission is produced by the presence of an active galactic nucleus (AGN). The exact proportion of AGN-dominated IR galaxies is actually not known, and the determination of such a ratio is one of the main problems of IR astronomy. A definitive AGN/star-forming galaxy separation requires the knowledge of the far-IR spectral energy distribution (SED) of these galaxies. Unfortunately, this is not possible for most high-z galaxies, as their far-IR emission is usually below the confusion limits at far-IR wavelengths (Dole et al. 2004). This separation is also complicated by the existence of mixed systems, where both star formation and AGN activity significantly contribute to the IR emission (e.g., Lutz et al. 2005; Yan et al. 2005; Le Floc'h et al. 2007). However, the AGN discrimination is essential to disentangle how much of the IR energy density is associated with star formation.

The study of a galaxy luminosity function (LF) at different redshifts allows us to understand the composition of the extragalactic background as a function of look-back time. The analysis of the changes of the LF with redshift is one of the most direct methods to explore the evolution of a galaxy population. The first studies of the IR galaxy LF in the local universe and at low ($z \lesssim 1$) redshifts have been based on *IRAS* and *ISO* data (e.g., Saunders et al. 1990; Xu 2000; Takeuchi et al. 2003, 2006; Pozzi et al. 2004; Serjeant et al. 2004). Using the most recent *Spitzer* MIPS data, Le Floc'h et al. (2005) analyzed in detail the evolution of the IR LF from $z = 0$ to ~ 1. They found a positive evolution in both luminosity and density between these two redshifts, implying that IR galaxies were more numerous and the IR output was dominated

[1] Institut d'Astrophysique Spatiale, F-91405 Orsay; Université Paris-Sud 11 and CNRS (UMR 8617), France.
[2] Current address: Institute of Astronomy, Swiss Federal Institute of Technology (ETH Hönggerberg), CH-8093 Zürich, Switzerland; caputi@phys.ethz.ch.
[3] *Spitzer* Science Center, California Institute of Technology, Pasadena, CA 91125.
[4] Institute for Astronomy, University of Hawaii, Honolulu, HI 96822.
[5] Astronomy Option, California Institute of Technology, Pasadena, CA 91125.

by brighter galaxies at $z \sim 1$ than at $z \sim 0$. The IR galaxy LFs at higher redshifts have been explored by other authors (Pérez-González et al. 2005; Babbedge et al. 2006).

Rest-frame 8 μm luminosities, in particular, are of main relevance for star-forming galaxies as they contain information on polycyclic aromatic hydrocarbon (PAH) emission. PAH molecules characterize star-forming regions (Désert et al. 1990), and the associated emission lines dominate the SED of star-forming galaxies between wavelengths $\lambda = 3.3$ and 17 μm, with a main bump located around 8 μm. Rest-frame 8 μm luminosities have been confirmed to be good indicators of knots of star formation (Roussel et al. 2001; Förster-Schreiber et al. 2004; Calzetti et al. 2005) and of the overall star formation activity of star-forming galaxies (e.g., Wu et al. 2005), except in low-luminosity galaxies with intense ultraviolet (UV) radiation fields (Galliano et al. 2005).

In this work we compute the rest-frame 8 μm LF at redshifts $z = 1$ and ~ 2, using 24 μm–selected galaxies in the two fields of the Great Observatories Origins Deep Survey (GOODS; Giavalisco et al. 2004). At $z \sim 2$, where the fraction of AGNs appears to be significant, we analyze separately the LFs for star-forming galaxies and for the total IR galaxy population. The two GOODS fields cover a smaller area than those analyzed by some other previous studies of the IR LF. However, they benefit from uniquely deep homogeneous photometric data sets, ranging from the X-rays to radio wavelengths, as well as an important spectroscopic coverage. As we explain in § 2, this makes possible an almost complete identification of 24 μm galaxies down to faint fluxes and the derivation of accurate redshift determinations (see also Caputi et al. 2006b, 2006c). These two characteristics are essential for a proper computation of the LF at high redshifts, without any conclusion relying on either completeness or selection function corrections.

The layout of this paper is as follows: In § 2 we describe in detail the selection of our 24 μm galaxy samples at redshifts $0.9 < z < 1.1$ and $1.7 < z < 2.3$. In § 3 we explain how we perform the separation between star-forming galaxies and AGNs within our sample. We compute the rest-frame 8 μm LF at $z = 1$ in § 4 and analyze its evolution from $z \sim 0$. In § 5 we present the rest-frame 8 μm LF at $z \sim 2$ and extend the analysis of the evolution up to this high redshift. Later, in § 6 we use a new empirical calibration based on *Spitzer* galaxies to obtain the bolometric IR LF at different redshifts. Finally, in §§ 7 and 8, respectively, we discuss our results and present some concluding remarks. We adopt throughout a cosmology with $H_0 = 70$ km s^{-1} Mpc^{-1}, $\Omega_M = 0.3$, and $\Omega_\Lambda = 0.7$.

2. THE IR GALAXY SAMPLE IN THE GOODS FIELDS

The GOODS fields, namely, the GOODS/Chandra Deep Field–South (GOODS/CDF-S) and GOODS/Hubble Deep Field–North (GOODS/HDF-N), have been observed by *Spitzer* as one of the Cycle 1 Legacy Science Programs (PI: Mark Dickinson). Extended areas of the CDF-S and HDF-N have also been observed as part of the *Spitzer* IRAC and MIPS Guaranteed Time Observers (GTO) programs (PI: Giovanni Fazio and George Rieke, respectively).

GOODS/IRAC maps at 3.6–8 μm and MIPS maps at 24 μm are now publicly available. The corresponding GOODS public 24 μm catalogs have been constructed using prior positional information from the IRAC 3.6 and 4.5 μm images and by an additional blind extraction of 24 μm sources. The resulting 24 μm catalogs are basically reliable and complete for galaxies with fluxes down to $S(24\ \mu\text{m}) = 80\ \mu$Jy (Chary et al. 2007, and see the *Spitzer* GOODS Web site[6]). For a comparison, we note that the 24 μm catalog constructed from the shallower MIPS/GTO observations

of the CDF-S achieves $\sim 80\%$ completeness and only has $\sim 2\%$ of spurious sources at a similar flux level (Papovich et al. 2004). Although, in principle, fainter sources can be detected in the deeper GOODS images, we decide to only use the conservative GOODS $S(24\ \mu\text{m}) > 80\ \mu$Jy galaxy catalogs for the selection of our 24 μm galaxy samples at $z \sim 1$ and ~ 2. In this way, our computed LFs are virtually not affected by incompleteness corrections (see §§ 4 and 5).

2.1. *Multiwavelength Analysis and Redshift Determinations for* 24 μm *Sources in the GOODS/CDF-S*

In the GOODS/CDF-S, we restrict our analysis to the 131 arcmin^2, which have deep J- and K_s-band coverage by the Infrared Spectrometer and Array Camera (ISAAC) on the "Antu" Very Large Telescope (Antu-VLT) (GOODS/EIS ver. 1.0 release; B. Vandame et al. 2007, in preparation). We used the $K_s < 21.5$ (Vega mag) galaxy catalog constructed by Caputi et al. (2006b) to identify the 24 μm galaxies in the GOODS/CDF-S catalog, using a matching radius of 2″. The percentage of 24 μm galaxies with double K_s-band identifications within this radius is only $\lesssim 8\%$, and 95% of the associations can be done restricting the matching radius to 1.5″ (Caputi et al. 2006a). In all cases of multiple identifications, we considered that the counterpart to the 24 μm source was the K_s galaxy closest to the 24 μm source centroid. The $K_s < 21.5$ mag catalog allows us to identify 515 24 μm galaxies within the 131 arcmin^2 area, i.e., $\sim 94\%$ of the 24 μm galaxies with $S(24\ \mu\text{m}) > 80\ \mu$Jy in this field.

Caputi et al. (2006b) measured multiwavelength photometry for all their $K_s < 21.5$ mag galaxies. They ran SExtractor (Bertin & Arnouts 1996) in "double-image mode" to perform aperture photometry on the GOODS/EIS version 1.0 J-band images, centered at the position of the K_s-band extracted sources. They also looked for counterparts of the $K_s < 21.5$ mag sources in the public GOODS Advanced Camera for Surveys (ACS) catalogs, which provided photometry in the B, V, I_{775}, and z bands. The stellarity parameter measured on the z-band images allowed them to separate out galactic stars. Finally, they ran SExtractor on the *Spitzer* IRAC 3.6 and 4.5 μm images to identify the $K_s < 21.5$ mag galaxies and measured aperture photometry at these longer wavelengths. We refer the reader to Caputi et al. (2006b) for additional details about the photometric measurements and applied aperture corrections.

Caputi et al. (2006b) obtained an estimated redshift for each one of their galaxies modeling their stellar SED from the B through the 4.5 μm bands. They used the public code HYPERZ (Bolzonella et al. 2000) with the GISSEL98 template library (Bruzual & Charlot 1993) and the Calzetti et al. (2000) reddening law to account for internal dust extinction.

The HYPERZ redshift estimates have been replaced by COMBO17 photometric redshifts (Wolf et al. 2004) for those galaxies with magnitudes $R < 23.5$ mag at redshift $z < 1$, which is the regime of higher accuracy for COMBO17. In these cases, the SED fitting has been constrained to the COMBO17 redshifts. The cross-correlation of the GOODS/CDF-S 24 μm catalog with the Caputi et al. (2006b) $K_s < 21.5$ mag catalog directly gives us estimated redshifts and best-fitting SED models for all the identified 24 μm galaxies.

2.2. *Multiwavelength Analysis and Redshift Determinations for* 24 μm *Sources in the GOODS/HDF-N*

In the GOODS/HDF-N, we followed a similar strategy for the analysis of sources as in the GOODS/CDF-S. However, unfortunately, we only have access to deep K_s-band data for a part of this field (Reddy et al. 2006a). Thus, we used the *Spitzer* IRAC 3.6 μm maps to identify the 24 μm galaxies. We analyzed

---

[6] Available at http://data.spitzer.caltech.edu/popular/goods.

in this case the entire GOODS/HDF-N region, i.e., the 160 arcmin^2 with deep GOODS/*Hubble Space Telescope* ACS coverage. We ran SExtractor on the IRAC 3.6 and 4.5 μm images. We constructed a catalog of 3.6 μm sources, accepting only those objects also identified in the 4.5 μm band. To encompass the technique applied by Caputi et al. (2006b) on the IRAC maps of the GOODS/CDF-S, we measured photometry in circular apertures of 2.83″ diameter[7] and applied aperture corrections of 0.50 and 0.55 mag to the 3.6 and 4.5 μm magnitudes, respectively. We then used this 3.6 μm catalog to identify the 24 μm sources in the GOODS/HDF-N, using a matching radius of 2″. This allows us to identify 856 24 μm galaxies in the 160 arcmin^2 of the GOODS/HDF-N, i.e., $\sim$95% of the 24 μm galaxies with $S(24 \; \mu m) > 80 \; \mu$Jy in this field. The identification completeness achieved for 24 μm galaxies in this field using 3.6 μm sources is similar to the identification completeness obtained for 24 μm galaxies in the GOODS/CDF-S using K_s-band sources. This indicates that the two identification methods are basically equivalent. In any case, the IRAC 3.6 and 4.5 μm data are incorporated in the SED modeling of all the sources in the two fields.

We followed up in the optical bands those IRAC 3.6 μm objects that were counterparts to $S(24 \; \mu m) > 80 \; \mu$Jy sources. Once more, we used the public GOODS ACS catalogs to obtain aperture photometry in the B, V, I_{775}, and z bands. In addition, we looked for counterparts of the 3.6 μm sources in the U- and HK'-band images of the GOODS/HDF-N (Capak et al. 2004). Although these images are relatively shallower than the other optical/near-IR data available for this field, we decided to include these data to improve the SED coverage. Finally, we incorporated the deep J- and K_s-band data from Reddy et al. (2006a) for those galaxies lying in the region where these data were available ($<$40% of the analyzed area).

We used the multiwavelength data from the U to the 4.5 μm bands to model the SED and obtain photometric redshifts for all of our 24 μm galaxies in the GOODS/HDF-N using HYPERZ, in an analogous way to that in Caputi et al. (2006b). As in the latter, we applied a set of criteria to control the HYPERZ output: (1) the photometric redshifts for galaxies detected in the shallow U-band catalogs were constrained to a maximum value $z_{phot} = 2$, as bright U-band sources are unlikely to be beyond these redshifts; (2) analogously, the estimated redshifts of galaxies not detected in the U band but detected in the B band were constrained to a maximum value $z_{phot} = 4$; (3) for the GOODS/HDF-N catalog, we found that HYPERZ produced an overdensity of galaxies in the redshift range $1.5 < z_{phot} < 1.7$. Comparison with spectroscopic redshifts (see below) suggested that this overdensity was an artifact of HYPERZ applied to our sample. Thus, to test these possible spurious redshifts, we double-checked the fitting of all the galaxies with HYPERZ redshift $1.5 < z_{phot} < 1.7$ using the PÉGASE library (Le Borgne & Rocca-Volmerange 2002). We kept the HYPERZ solution for those sources confirmed by PÉGASE as belonging to the 1.5–1.7 redshift range. For all the remaining $1.5 < z_{phot} < 1.7$ galaxies, we replaced the photometric redshift by the PÉGASE estimate. This strategy improved the agreement with spectroscopic redshifts. The percentage of galaxies with PÉGASE redshifts in our final 24 μm catalog for the GOODS/HDF-N is 5%.

2.3. *The Final IR Galaxy Samples in the Combined GOODS Fields*

Our final 24 μm catalog contains 1371 24 μm sources with $S(24 \; \mu m) > 80 \; \mu$Jy over a total area of 291 arcmin^2. We iden-
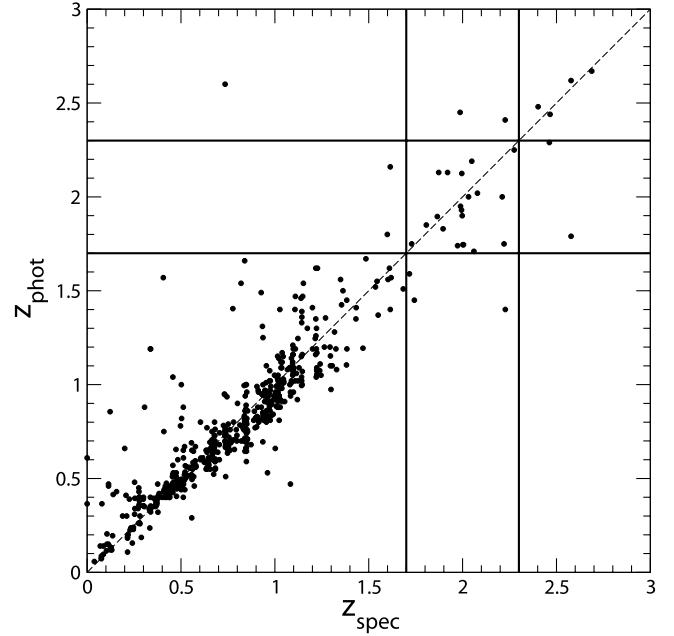
FIG. 1.—Comparison between photometric and spectroscopic redshifts for galaxies in our 24 μm–selected sample in the GOODS fields. The distribution of relative errors $dz = (z_{phot} - z_{spec})/(1 + z_{spec})$ has a median -0.007 and a dispersion $\sigma_z = 0.05$. The horizontal lines separate the galaxies with $1.7 < z_{phot} < 2.3$, and the vertical lines those with $1.7 < z_{spec} < 2.3$. The distribution of relative errors for the $1.7 < z_{spec} < 2.3$ subsample of galaxies has a median -0.01 and a dispersion $\sigma_z = 0.06$.

tified only 22 out of 1371 sources as galactic stars. All the remaining sources are galaxies. Our aim is to separate two subsamples of galaxies from this final catalog: (1) the 24 μm galaxies with redshifts $0.9 < z < 1.1$ for the computation of the IR LF at $z = 1$, and (2) the 24 μm galaxies with redshifts $1.7 < z < 2.3$ for the computation of the IR LF at $z \sim 2$.

We performed a final step before separating the two definitive subsamples of 24 μm galaxies used in this work. In addition to the wealth of photometric data, both GOODS fields benefit from an important amount of spectroscopic data, most of which are publicly available (Cohen et al. 1996; Le Fèvre et al. 2004; Wirth et al. 2004; Vanzella et al. 2005, 2006; P. I. Choi et al. 2007, in preparation; among others). Some additional redshifts in the GOODS/CDF-S have been kindly made available to us by François Hammer and Héctor Flores. We compiled these data and found that more than 45% of our 24 μm galaxies in the combined fields had spectroscopic redshifts. We incorporated these spectroscopic redshifts into our catalog, which superseded the corresponding photometric values. The finally discarded photometric redshifts have been used to assess the quality of our redshift estimates. Figure 1 shows the comparison between photometric and spectroscopic redshifts for the galaxies in our sample for which both redshifts are available. We observe a good agreement between photometric estimates and real redshifts. The distribution of relative errors $dz = (z_{phot} - z_{spec})/(1 + z_{spec})$ has a median value -0.007 and the dispersion is $\sigma_z = 0.05$.

From the definitive redshift catalog that incorporates spectroscopic redshifts, we select those 24 μm galaxies lying at $0.9 < z < 1.1$ and $1.7 < z < 2.3$.

The $0.9 < z < 1.1$ sample is composed of 227 galaxies with $S(24 \; \mu m) > 80 \; \mu$Jy and a median redshift $z = 1.00$. We use this sample to compute the IR LF at $z = 1$. More than 60% of these galaxies have spectroscopic redshifts z_{spec}. The quality of photometric redshifts is similar to that for the total sample: the
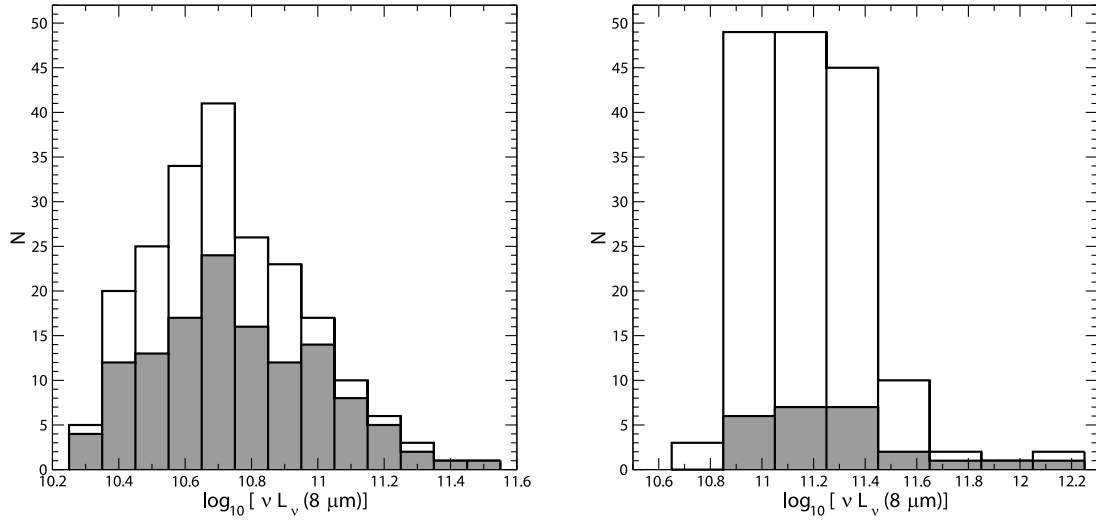
FIG. 2.—Distribution of rest-frame 8 μm luminosities for galaxies at redshifts $0.9 < z < 1.1$ (*left*) and $1.7 < z < 2.3$ (*right*). In each panel, the open and shaded histograms include all the galaxies and only those with spectroscopic redshifts, respectively.

median of relative errors $dz = (z_{\mathrm{phot}} - z_{\mathrm{spec}})/(1 + z_{\mathrm{spec}})$ is -0.01 and the dispersion is $\sigma_z = 0.05$. In the computation of the IR LF at $z = 1$, we consider that these errors only affect those galaxies with photometric redshifts ($<40\%$).

Our $1.7 < z < 2.3$ sample contains 161 24 μm galaxies with $S(24\ \mu\mathrm{m}) > 80\ \mu\mathrm{Jy}$. This is the sample we use to compute the IR LF at redshift $z \sim 2$. The median redshift of these 161 galaxies is $z = 1.93$. Although for practicality we refer to these galaxies as the $z \sim 2$ sample, all the calculations made in §§ 5 and 6 take into account the actual median redshift value. More than 15% of the galaxies selected with $1.7 < z < 2.3$ have spectroscopic redshifts. The quality of photometric redshifts for the $z \sim 2$ sample can also be assessed from Figure 1. We see that the agreement between photometric and spectroscopic redshifts is still very reasonable for this high-redshift sample. The distribution of relative errors $dz = (z_{\mathrm{phot}} - z_{\mathrm{spec}})/(1 + z_{\mathrm{spec}})$ has a median -0.01 and a dispersion $\sigma_z = 0.06$. This statistics has been computed based on all sources (i.e., AGNs included; see below). This suggests that the SED templates we use to derive photometric redshifts are suitable for all our sample. The photometric redshift error bars affect the majority of galaxies in our $z \sim 2$ sample and are taken into account in the computation of the corresponding LF, as we explain in § 5.

We note that the galaxies with spectroscopic redshifts are representative of our entire 24 μm sample in each of the considered redshift bins ($0.9 < z < 1.1$ and $1.7 < z < 2.3$). The two panels in Figure 2 show the rest-frame 8 μm luminosities of all of our galaxies (*open histograms*) and those of galaxies with spectroscopic redshifts (*shaded histograms*), at these different redshifts. Details on the calculation of 8 μm luminosities are given in § 4. From Figure 2, we can see that galaxies with spectroscopic redshifts basically span the whole range of IR luminosities considered in this work. Thus, the errors derived from the comparison of photometric and spectroscopic redshifts are applicable to the entire IR LF.

3. THE NORMAL/ACTIVE GALAXY SEPARATION

In this work we would like to compare the IR LF for starforming galaxies only with the total IR LF. To do this, we need to identify the active galaxies present in our sample.

One of the most efficient ways of identifying AGNs is through their X-ray emission. The GOODS fields have deep X-ray coverage obtained with the *Chandra X-Ray Observatory*: the 1 Ms maps for the CDF-S (Giacconi et al. 2002) and the 2 Ms maps for the HDF-N (Alexander et al. 2003). We used the corresponding public X-ray catalogs to identify the AGNs within our sample. However, given the depth of these catalogs (especially that of the HDF-N), X-ray sources include not only quasars and AGNs but also powerful starbursts that also emit in X-rays. To separate the two classes of X-ray sources, an optical versus X-ray flux diagram can be used. Figure 3 shows the R-band magnitude versus the soft X-ray flux of the X-ray–detected galaxies in our 24 μm sample in

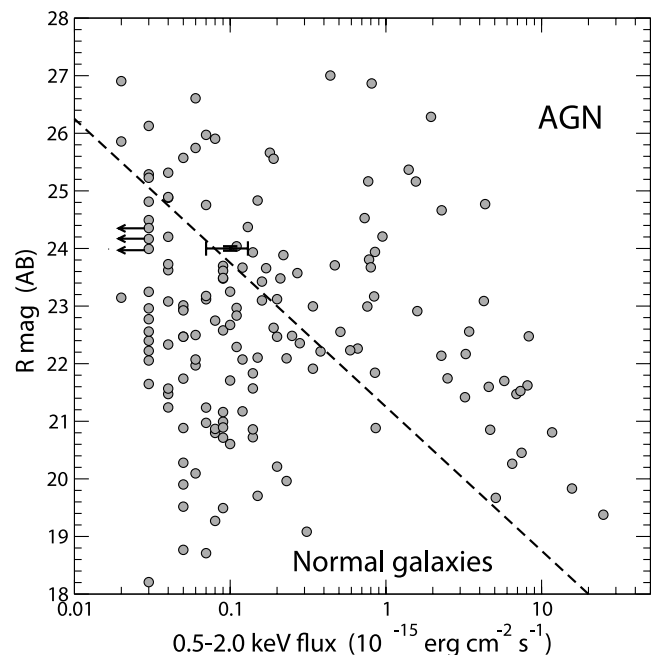
FIG. 3.—R-band magnitudes vs. soft X-ray fluxes for the X-ray-detected galaxies in our 24 μm galaxy sample in the GOODS/HDF-N. The error bar for a generic source with soft X-ray flux 10^{-16} ergs cm^{-2} s^{-1} and $R = 24$ mag is shown. The left-pointing arrows indicate that the soft X-ray flux 3×10^{-17} ergs cm^{-2} s^{-1} is an upper limit.
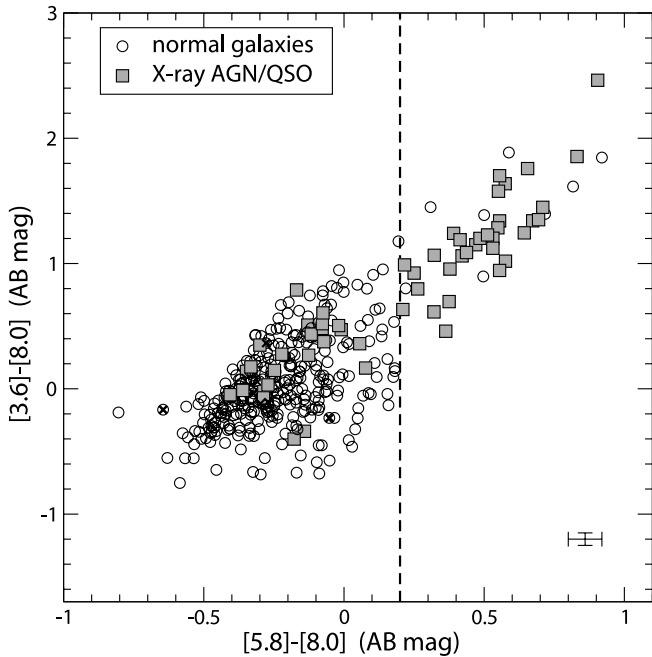
FIG. 4.—IRAC-based color-color diagram for the 24 μm sources with redshifts $z > 1.5$ in the GOODS fields. Filled squares and open circles refer to X-ray–classified AGNs and to all the other $z > 1.5$ 24 μm galaxies, respectively. The crosses indicate the few star-forming galaxies at $z > 1.5$ that are X-ray detected. The typical error bars for the colors of these sources are indicated in the lower right corner of the plot.

the HDF-N. The R-band magnitudes of our galaxies have been interpolated using the V and I_{775} magnitudes. This plot is similar to that presented in Alexander et al. (2003). The dashed line shows the empirical separation between normal galaxies and AGNs, as calibrated by Hornschemeier et al. (2001). Using this diagram, we identify the X-ray–detected AGNs within our 24 μm sample and, in particular, those at $0.9 < z < 1.1$ and $1.7 < z < 2.3$.

Some AGNs with weak soft X-ray fluxes but significant emission in the hard bands can contaminate the normal galaxy region in the R-band magnitude versus soft X-ray flux diagram. These AGNs are characterized by a flat photon index $\Gamma < 1.0$ (e.g., Hornschemeier et al. 2003). We also looked for these kinds of objects to identify the AGNs present in our sample.

It is known, however, that the X-ray selection can be incomplete for the selection of AGNs. Other active galaxies exist, which are not detected even in deep X-ray surveys. A complementary method to select active galaxies can be developed based on the analysis of the IR color excess in the *Spitzer* IRAC bands. Figure 4 shows the [3.6 μm] − [8 μm] versus [5.8 μm] − [8 μm] colors for all the galaxies with redshift $z > 1.5$ in our 24 μm sample. Open circles correspond to all those galaxies not classified as AGNs using X-ray data (either not detected in X-rays or X-ray sources classified as starbursts). Filled squares indicate the X-ray–classified AGNs. We restrict this diagram to high-redshift sources for the following reason. The stellar bump centered at rest-frame wavelength $\lambda \sim 1.6$ μm is shifted into the IRAC bands at $z \gtrsim 1.5$. For active galaxies, the galaxy SED at the same rest-frame wavelengths is dominated by a power-law continuum. Thus, it is expected that an IRAC-based color-color diagram is able to separate the AGNs through their IR excess. At low redshifts, this separation is much less clear, especially because star-forming galaxies with PAH emission can mimic the IR excess. Similar color-color plots have

been used with the purpose of separating normal and active galaxies elsewhere (e.g., Lacy et al. 2004; Stern et al. 2005; Caputi et al. 2006a).

Inspection of Figure 4 shows that X-ray–selected AGNs display a wide range of [3.6 μm] − [8 μm] and [5.8 μm] − [8 μm] colors, while the vast majority of "normal galaxies" (i.e., non–X-ray–classified AGNs) appear on the left-hand side of this diagram, with a color [5.8 μm] − [8 μm] $\lesssim 0.2$ (AB). As we mentioned above, the relatively blue colors are produced by the stellar SED bump mapped at the IRAC wavelengths. The galaxies lying on the right-hand side, on the contrary, present an excess in the SED continuum that is characteristic of AGNs. Thus, based on this diagram, we adopt an empirical color cut to produce an additional AGN selection criterion: all the $z > 1.5$ galaxies with [5.8 μm] − [8 μm] > 0.2 (AB) within our sample are classified as AGNs. This same additional AGN selection criterion has been used by Caputi et al. (2006a).

We would like to note that while this color cut produces a safe criterion to select additional active galaxies, it is possibly not complete. The dispersion of colors displayed by X-ray–selected AGNs suggests that other active sources, not detected in X-rays and with no IRAC color excess, could also exist among the 24 μm galaxies. On the other hand, some of the X-ray–classified AGNs could be composite systems, where a fraction of the bolometric IR luminosity is actually due to star formation. Unfortunately, no AGN selection criterion appears to be both complete and reliable at the same time (e.g., Barmby et al. 2006). As we do not have information on the far-IR emission of our galaxies, our separation criteria are possibly the most adequate to discriminate AGNs.

For our sample of 227 24 μm galaxies with redshift $0.9 < z < 1.1$, only the X-ray criteria have been applied. We identify 23 out of 227 galaxies as AGNs, i.e., $\sim 10\%$ of the sample. We exclude the AGNs from our sample in order to determine the IR LF for star-forming galaxies at $z = 1$, but we note that the inclusion of AGNs only has a minor impact on the LF at this redshift.

For the sample at redshifts $1.7 < z < 2.3$, we applied both selection criteria to separate AGNs (X-ray and IRAC color classifications). The fraction of active galaxies at these redshifts appears to be more important than at $z \sim 1$. We identify 29 AGNs among our 161 24 μm galaxies at $1.7 < z < 2.3$, i.e., $\sim 18\%$ of the sample. A total of 23 out of these 29 AGNs have been identified using X-rays, and the remaining 6 AGNs have been classified through their IRAC colors. As seen below, the LFs computed including and excluding AGNs have nonnegligible differences because these objects dominate the bright end of the IR LF at these high redshifts. Throughout this paper, when we refer to the star-forming galaxies at redshift $z \sim 2$, we mean our sample of $161 − 29 = 132$ objects that we have not classified as AGNs at these redshifts.

4. THE REST-FRAME 8 μm LF AT REDSHIFT $z = 1$

4.1. *The k-Corrections from* 11.4–12.7 *to* 8 μm

Before computing the rest-frame 8 μm LF at $z \sim 2$, we aim to understand its evolution from $z \sim 0$ to redshift $z = 1$. For this, we compute the rest-frame 8 μm LF for our 204 24 μm–selected star-forming galaxies in the redshift range $0.9 < z < 1.1$. AGNs have been excluded from this analysis. AGNs constitute $\sim 10\%$ of our sample with $0.9 < z < 1.1$, and their exclusion does not significantly change the shape of the 8 μm LF at $z = 1$. This is in contrast to what we find at $z \sim 2$, where AGNs constitute a somewhat higher fraction of sources that dominate the bright end of the rest-frame 8 μm LF (see § 5).
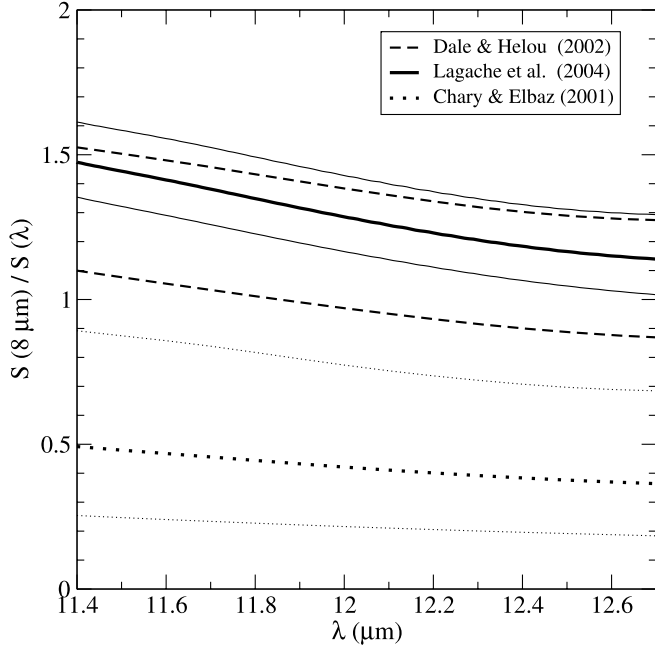
Fig. 5.—The k-corrections between 11.4–12.7 and 8 μm fluxes obtained using different IR galaxy model templates: Lagache et al. (2004; *solid lines*), Chary & Elbaz (2001; *dotted lines*), and Dale & Helou (2002; *dashed lines*). The thin solid and dotted lines indicate the interval of corrections obtained using the different models of Lagache et al. (2004) and Chary & Elbaz (2001), respectively, with bolometric IR luminosity $L_{IR} > 10^{11}$ $L_{\odot}$. The corresponding thick lines indicate median k-corrections. The dashed line corresponds to the Dale & Helou (2002) model with parameter $\alpha = 1.1$ and 1.4.

We compute the rest-frame 8 μm luminosity ($\nu L_{\nu}^{8\,\mu m}$) of each galaxy as $\nu L_{\nu}^{8\,\mu m} = \nu 4\pi k(\lambda_{rf})S(24\,\mu m)d_L^2(z)$, where $S(24\,\mu m)$ is the 24 μm flux, $d_L(z)$ is the luminosity distance, and $k(\lambda_{rf})$ is the corresponding k-correction at the rest-frame wavelength λ_{rf}. The width of the redshift bin we consider, $0.9 < z < 1.1$, implies that the observed 24 μm maps rest-frame wavelengths 11.4 μm $< \lambda_{rf} < 12.7$ μm. We need then to apply k-corrections to convert the rest-frame 11.4–12.7 μm into 8 μm fluxes.

To compute these k-corrections, we analyze different sets of IR galaxy templates available in the literature, namely, the models by Chary & Elbaz (2001) and Elbaz et al. (2002), Dale et al. (2001) and Dale & Helou (2002), and Lagache et al. (2004). We convolve the SED templates in all these models with the transmission function of the 24 μm filter and obtain the relation between the fluxes at 11.4–12.7 and 8 μm. Figure 5 shows the λ–to–8 μm k-corrections in the wavelength range $\lambda_{rf} = 11.4$–12.7 μm. Different line styles indicate the k-corrections obtained with different SED templates. The solid and dotted lines correspond to the range of k-corrections derived for galaxies with bolometric IR luminosities $L_{IR} > 10^{11}$ $L_{\odot}$, from the Lagache et al. (2004) and Chary & Elbaz (2001) models, respectively (with thick lines indicating the median values). The dashed lines show the k-corrections obtained with the Dale et al. (2001) SED model with parameters $\alpha = 1.1$ and 1.4 (see Dale et al. 2001). It is clear from inspection of Figure 5 that the k-corrections between 11.4–12.7 and 8 μm obtained with these different models have some significant dispersion. These differences are produced by the limited knowledge on PAH emission when modeling the PAH-dominated region of a star-forming galaxy SED.

In this work we adopt the median k-corrections obtained with the Lagache et al. (2004) models of star-forming galaxies with bolometric IR luminosities $L_{IR} > 10^{11}$ $L_{\odot}$ (*thick solid line in* Fig. 5). As we show in § 6.1.2, the Lagache et al. (2004) tem-

plates produce an 8 μm–to–bolometric IR luminosity conversion quite close to that measured on the observed SED of *Spitzer* galaxies (Bavouzet et al. 2006). This suggests that these templates incorporate an adequate modeling of the PAH emission region in the star-forming galaxy SED.

4.2. *The* $1/V_{max}$ *Method*

We compute the rest-frame 8 μm LF for star-forming galaxies at redshift $z = 1$ using the $1/V_{max}$ method (Schmidt 1968). For this calculation, we consider the 204 star-forming galaxies with redshift $0.9 < z < 1.1$ within our sample. The advantage of the $1/V_{max}$ technique is that it allows us to compute the LF directly from the data, with no parameter dependence or model assumption. Besides, the normalization of the LF is directly obtained from the same calculation. The comoving volume $V_{max} = V_{z_{max}} - V(z = 0.9)$ for each source corresponds to the maximum redshift z_{max} at which it would be included in the catalog, given the limiting flux $S(24\,\mu m) = 80$ μJy, and provided that this redshift is smaller than the maximum of the considered redshift bin (in this case $z = 1.1$). Otherwise, V_{max} is equal to the volume corresponding to the $0.9 < z < 1.1$ bin $V_{max} = V_{bin}$.

As we explained in § 2, the GOODS 24 μm catalogs are basically complete down to the limiting flux and, thus, no sample completeness corrections are needed for our catalogs. However, we do apply completeness corrections to account for the percentage (5%–6%) of unidentified 24 μm sources (see § 2). These identification completeness corrections are very small, and none of the conclusions presented here depend on the application of such corrections.

We present the results of our rest-frame 8 μm LF at redshift $z = 1$ computed with the $1/V_{max}$ method in Figure 6 (*triangles*) and Table 1. This LF, as well as all the others presented in this work, has been computed jointly on the GOODS/CDF-S and GOODS/HDF-N. Although we have checked the consistency within the error bars of the LF obtained in the two fields separately, the sample variance effects are more important than when considering both fields combined (see Fig. 9). We show the 8 μm LF function computed with the $1/V_{max}$ method only in the completeness region of 8 μm luminosities ($\nu L_{\nu}^{8\,\mu m} \gtrsim 3 \times 10^{10}$ $L_{\odot}$), imposed by the flux limits of the 24 μm survey and the considered redshifts. The total comoving volume probed by our survey is 1.3×10^5 Mpc^3.

The error bars for these LF values depend not only on the number of sources (Poisson statistics) but also on the errors in the photometric redshifts and in the k-corrections applied. The errors in the photometric redshifts affect only <40% of our galaxies at $0.9 < z < 1.1$, given the high percentage of available spectroscopic redshifts. To account for the errors in the photometric redshifts, we made Monte Carlo simulations of our $\nu L_{\nu}^{8\,\mu m}$ catalogs. We produced 1000 simulated catalogs, each one with the same number of sources as our original $0.9 < z < 1.1$ catalog of star-forming galaxies (i.e., 204 sources each). The redshift of each source has been allowed to randomly vary following a Gaussian distribution centered at $z_{center} = z - 0.01$ and with a dispersion $\sigma_z = 0.05(1 + z)$ (see § 2.3), where z is the redshift of the source in the original catalog. The redshift of those sources with spectroscopic determinations has been left unchanged. For the k-corrections, we fixed the error bars to $\epsilon = 0.50$, which is roughly the dispersion between the different Lagache et al. (2004) and Dale & Helou (2002) model predictions (see Fig. 5). To include these errors in the simulations, we computed the rest-frame 8 μm luminosity $\nu L_{\nu}^{8\,\mu m}$ of each galaxy in the mock catalog allowing
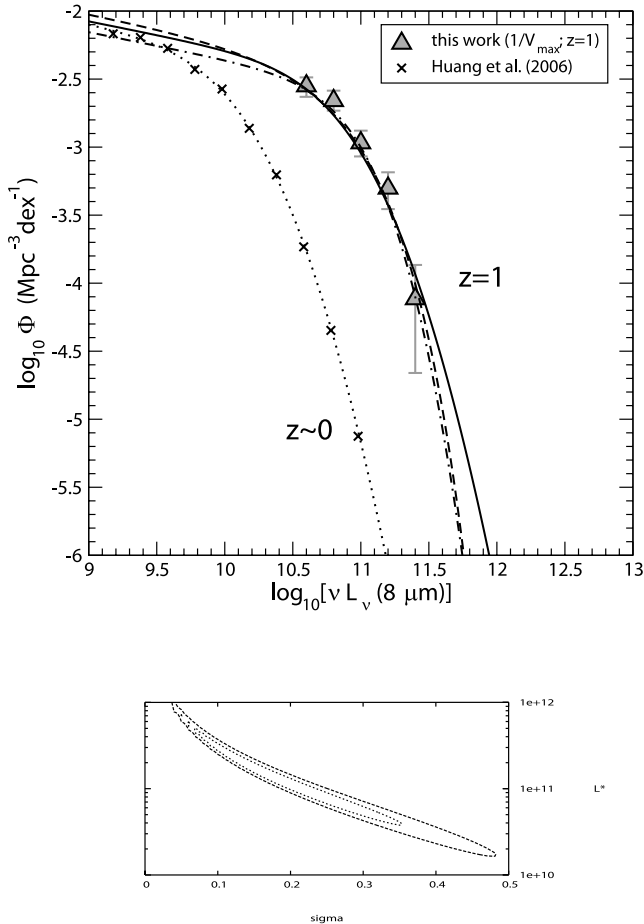
TABLE 1
THE REST-FRAME 8 μm LF FOR STAR-FORMING GALAXIES
AT $z = 1$ OBTAINED WITH THE $1/V_{\max}$ METHOD

$\log_{10}(\nu L_\nu^{8\,\mu m})$	$\log_{10}\Phi(\mathrm{Mpc}^{-3}\,\mathrm{dex}^{-1})$
10.60....................	$-2.55^{+0.06}_{-0.08}$
10.80....................	$-2.66^{+0.07}_{-0.07}$
11.00....................	$-2.97^{+0.09}_{-0.10}$
11.20....................	$-3.30^{+0.12}_{-0.15}$
11.40....................	$-4.12^{+0.25}_{-0.54}$

4.3. *The Maximum Likelihood Analysis*

The shape of the $z \sim 0$ LF can be fitted with a double exponential function (Saunders et al. 1990; Pozzi et al. 2004; Le Floc'h et al. 2005):

$$\Phi(L)d\log_{10}(L) = \Phi^*\left(\frac{L}{L^*}\right)^{1-\alpha}$$
$$\times \exp\left[-\frac{1}{2\sigma^2}\log_{10}^2\left(1 + \frac{L}{L^*}\right)\right]d\log_{10}(L), \quad (1)$$

where, in this case, $L \equiv \nu L_\nu^{8\,\mu m}$. The parameters α and $1/\sigma^2$ correspond to the slopes at the faint and the bright ends, respectively. L^* is the characteristic $\nu L_\nu^{*8\,\mu m}$ luminosity where the transition between the faint and bright regimes occurs, and Φ^* is the normalization factor. Usually, the parameter α is fixed a priori, as the faint end of the LF is poorly constrained. Fixing $\alpha = 1.2$ (e.g., Zheng et al. 2006) and using a χ^2 minimization technique, we obtain that the best-fitting parameters for the LF at $z \sim 0$ are $\sigma = 0.36 \pm 0.01$, $L^* = (5.8 \pm 0.2) \times 10^9 L_\odot$, and $\Phi^* = (5.7 \pm 0.1) \times 10^{-3}$ Mpc^{-3} dex^{-1}. The resulting curve (*dotted line in* Fig. 6) produces an excellent fitting of the $1/V_{\max}$ LF at $z \sim 0$.

Assuming that the form given in equation (1) is also suitable to describe the IR LF for star-forming galaxies at higher redshifts, we obtain a second independent calculation of the rest-frame 8 μm LF at redshift $z = 1$ using the STY (Sandage et al. 1979) maximum likelihood (ML) analysis. This is a parametric technique that assumes a given shape for the LF. No data binning is involved in the calculation. The advantage of the ML analysis over the $1/V_{\max}$ technique is that the former does not contain any assumption on a uniform spatial distribution of galaxies. The corresponding likelihood estimator reads

$$\mathcal{L}\left[s_k | (z_i, L_i)_{i=1,\ldots,N}\right] = \prod_{i=1}^{N}\left[\frac{\Phi(s_k, L)}{\int_{\log_{10}(Li0)}^{+\infty}\Phi(s_k, L)d\log_{10}(L)}\right]^{w_i}, \quad (2)$$

where the product is made over the $i = 1, \ldots, N$ galaxies of the sample. Here $\Phi(s_k, L)$ is the adopted form for the LF as a function of the luminosity L, and which depends on the parameters s_k, and L_0^i is the minimum luminosity at which the ith galaxy would be observable, given its redshift z_i and the flux limit of the survey. The weighting factors w_i allow us to take into account completeness corrections (Zucca et al. 1994; Ilbert et al. 2005). By maximizing $\mathcal{L}$ (or, for simplicity, its logarithm), one can obtain the values of the parameters s_k yielding the ML. The normalization factor Φ^* is recovered after the maximization, by integrating the obtained ML LF without normalization in the range of luminosities of the survey, and making it equal to the number density of observed galaxies. We note that the ML analysis provides a direct calculation of the LF (i.e., it does not constitute a fitting

FIG. 6.—*Top*: Rest-frame 8 μm LF for star-forming galaxies at $z = 1$ in the GOODS fields, compared to the 8 μm LF at $z \sim 0$. The crosses show the 8 μm LF for star-forming galaxies at $z \sim 0$, as computed by Huang et al. (2006) with the $1/V_{\max}$ method. The dotted line represents the best χ^2 fit obtained using a double exponential function as that in eq. (1). The triangles show the $1/V_{\max}$ LF at $z = 1$ obtained in this work, only strictly in the region of completeness of 8 μm luminosities. Lines of different styles show the 8 μm LF at $z = 1$ computed with the ML STY analysis, assuming different laws: a double exponential form with bright-end slope fixed to the local value ($\sigma = 0.36$; *solid line*), the same double exponential form with a free σ parameter (*dot-dashed line*), and a Schechter function (*dashed line*). *Bottom*: The 68.3% and 95.4% confidence levels in (σ, $\nu L_\nu^{*8\,\mu m}$)-space in the case of a double exponential law with σ as a free parameter. The parameter values yielding the ML are $\sigma = 0.20^{+0.11}_{-0.07}$ and $L^* \equiv \nu L_\nu^{*8\,\mu m} = (1.32^{+1.31}_{-0.74}) \times 10^{11} L_\odot$.

the corresponding k-correction to have a random value within the range of its error bar. Finally, the LF has been recomputed with the $1/V_{\max}$ method for each of the mock catalogs, with exactly the same procedure as for the original catalog. From the distribution of the LF values in each $\nu L_\nu^{8\,\mu m}$ bin, we determined the error bars on our original $1/V_{\max}$ results.

For a comparison, we also show the 8 μm LF of star-forming galaxies at redshift $z \sim 0$ (strictly $0 < z < 0.3$, with median $z \approx 0.2$), computed by Huang et al. (2006), using the $1/V_{\max}$ method applied to IRAC 8 μm GTO data (*crosses in* Fig. 6). No error bars have been plotted for this LF, as they are significantly smaller than the error bars of the LF we determine here. The comparison of this $1/V_{\max}$ LF with our own determination at $z = 1$ shows a substantial increment of the density of star-forming galaxies with rest-frame 8 μm luminosities $\log_{10}(\nu L_\nu^{8\,\mu m}) \gtrsim 10.5$, with increasing redshift. We note that this behavior is evident from the $1/V_{\max}$ calculation, independently of the parametric analysis we discuss below.

Functional Form	α	σ	$\nu L_\nu^{*8\,\mu m}$ ($L_\odot$)	Φ^* (Mpc^{-3} dex^{-1})
Double exponential (eq. [1])	1.2 (fixed)	0.36 (fixed)	$(3.55^{+0.52}_{-0.40}) \times 10^{10}$	$(3.95^{+0.50}_{-0.49}) \times 10^{-3}$
	1.2 (fixed)	$0.20^{+0.11}_{-0.07}$ (free)	$(1.10^{+0.99}_{-0.64}) \times 10^{11}$	$(2.54^{+0.60}_{-0.35}) \times 10^{-3}$
Schechter (eq. [3])	1.2 (fixed)	...	$(7.2^{+0.9}_{-0.7}) \times 10^{10}$	$(3.88^{+0.46}_{-0.41}) \times 10^{-3}$

procedure as the χ^2 minimization) and is completely independent of the LF obtained with the $1/V_{\max}$ technique.

For the case of our rest-frame 8 μm LF at $z = 1$, we apply the STY method using equation (1) and fixing the slopes at the faint and bright ends to the same values as at $z \sim 0$, i.e., $\alpha = 1.2$ and $\sigma = 0.36$, respectively. In this case, we obtain that the value of the characteristic luminosity that maximizes the likelihood estimator is $L^* \equiv \nu L_\nu^{*8\,\mu m} = (3.55^{+0.52}_{-0.40}) \times 10^{10}\ L_\odot$, and the derived normalization factor is $\Phi^* = (3.95^{+0.50}_{-0.49}) \times 10^{-3}$ Mpc^{-3} dex^{-1}. The error bars on L^* have been computed considering $\Delta(\ln \mathcal{L}) = -0.5$ and the uncertainties derived from the Monte Carlo simulations. The degeneracies in parameter space given by $\Delta(\ln \mathcal{L}) = -0.5$ dominate the L^* error budget. The error bars on Φ^* have been derived using the extreme values of L^* (i.e., L^* plus or minus its error). The resulting curve for the ML LF at $z = 1$, obtained with a double exponential law with $\sigma = 0.36$, is indicated with a solid line in the top panel of Figure 6 (see also Table 2).

Another possibility is to allow the slope at the bright end ($1/\sigma^2$) to be a free parameter in the ML analysis. Doing so, we obtain that the ML is produced for $\sigma = 0.20^{+0.11}_{-0.07}$, $L^* \equiv \nu L_\nu^{*8\,\mu m} = (1.10^{+0.99}_{-0.64}) \times 10^{11}\ L_\odot$, and the derived normalization is $\Phi^* = (2.54^{+0.60}_{-0.35}) \times 10^{-3}$ Mpc^{-3} dex^{-1} (*dot-dashed line in* Fig. 6, *top panel*). The degeneracy in (σ, L^*)-space is shown in the bottom panel of this figure.

The LF obtained with the ML analysis, in the case of both a free σ-value and fixed $\sigma = 0.36$, is in good agreement with the LF computed with the $1/V_{\max}$ method. This confirms that the double exponential law in equation (1) also provides a good description of the 8 μm LF at high redshifts. The degeneracy existing in the σ-value is due to the limited constraint that our data can put on the bright end of the LF at $z = 1$. In Figure 6 we see that the double exponential forms with $\sigma = 0.20$ and 0.36 only differ significantly at the very bright end of the LF ($\nu L_\nu^{8\,\mu m} \gtrsim 10^{11.5}\ L_\odot$ at $z = 1$). Large-area surveys with a significant number of very bright IR galaxies, as, for example, the ~ 2 deg^2 *Spitzer* COSMOS survey (Sanders et al. 2007), are necessary to set tighter constraints in (σ, L^*)-space.

Finally, we explore whether other functional forms could also be suitable to describe the rest-frame 8 μm LF at $z = 1$. We repeat the calculation of the LF with the STY method, but this time using a Schechter (1976) function:

$$\Phi(L)d \log_{10}(L) = \Phi^* \left(\frac{L}{L^*}\right)^{1-\alpha} \exp\left(-\frac{L}{L^*}\right) d \log_{10}(L). \quad (3)$$

By fixing $\alpha = 1.2$, we find that the ML is obtained for a characteristic luminosity $L^* \equiv \nu L_\nu^{*8\,\mu m} = (7.2^{+0.9}_{-0.7}) \times 10^{10}\ L_\odot$ and the derived normalization is $\Phi^* = (3.88^{+0.46}_{-0.41}) \times 10^{-3}$ Mpc^{-3} dex^{-1}. The resulting ML curve is shown with a dashed line in Figure 6. The Schechter form actually produces an LF quite close to that obtained with the $\sigma = 0.20$ double exponential form, within the observed luminosity range of our survey.

The degeneracy existing in the shape of the IR LF, as constrained from our data, produces some uncertainty in the determination of the number density of the most luminous IR galaxies (see Table 5). However, as we discuss below, this degeneracy has little impact on the derived luminosity density. This value is mainly governed by the turnover of the LF, which we can properly determine here, given the depth of our survey.

4.4. The Evolution of the Rest-Frame 8 μm LF from $z \sim 0$ to $z = 1$

When using the same law to describe the rest-frame 8 μm LF at both redshifts $z \sim 0$ and $z = 1$, the differences found in the characteristic luminosity L^* and the normalization parameter Φ^* can be understood as a luminosity and density evolution:

$$L^*(z_2 = 1) = L^*(z_1 \sim 0)\left(\frac{1+z_2}{1+z_1}\right)^{\gamma_L},$$

$$\Phi^*(z_2 = 1) = \Phi^*(z_1 \sim 0)\left(\frac{1+z_2}{1+z_1}\right)^{\gamma_\delta}, \quad (4)$$

where we strictly use $z_1 = 0.2$ (the median redshift of the Huang et al. [2006] sample). Parameters γ_L and γ_δ describe the evolution of the L^* and Φ^* parameters with redshift. The values of these parameters at $z \sim 0$ and $z = 1$, corresponding in both cases to a double exponential with $\sigma = 0.36$, produce (see § 4.3)

$$\gamma_L = 3.5 \pm 0.4,$$
$$\gamma_\delta = -0.7 \pm 0.1. \quad (5)$$

This implies a strong positive-luminosity evolution and a mild negative-density evolution between $z \sim 0$ and $z = 1$. The mild negative-density evolution to $z = 1$ refers to the overall normalization Φ^*. However, it is clear from Figure 6 that, within the 8 μm luminosity range spanned by our sample, the density of galaxies at $z = 1$ is larger than that at $z \sim 0$. This is consistent with what has been found by Le Floc'h et al. (2005) from the analysis of the rest-frame 15 μm LF and confirms, once more, the increasing importance of IR galaxies up to redshift $z \sim 1$. For clarity, the densities of galaxies we obtain by integrating the rest-frame 8 μm LF above different luminosity cuts at different redshifts are shown in Table 5.

By integrating the LF weighted by the luminosity values, over all luminosities, we can obtain the total rest-frame 8 μm luminosity density. In fact, for the obtention of the total luminosity density, the precise limits of integration are irrelevant, provided that the turnover of the LF is completely contained within these limits. Moreover, the use of any of the different laws that are suitable to describe the LF (see § 4.3) produces basically the same value for the luminosity density, as all of them are in close agreement around the turnover.

At $z = 1$, we find that the total rest-frame 8 μm luminosity density is $(1.4 \pm 0.1) \times 10^8$, $(1.3 \pm 0.1) \times 10^8$, and $(1.4 \pm 0.1) \times 10^8\ L_\odot$ Mpc^{-3} for the cases of a double exponential law with
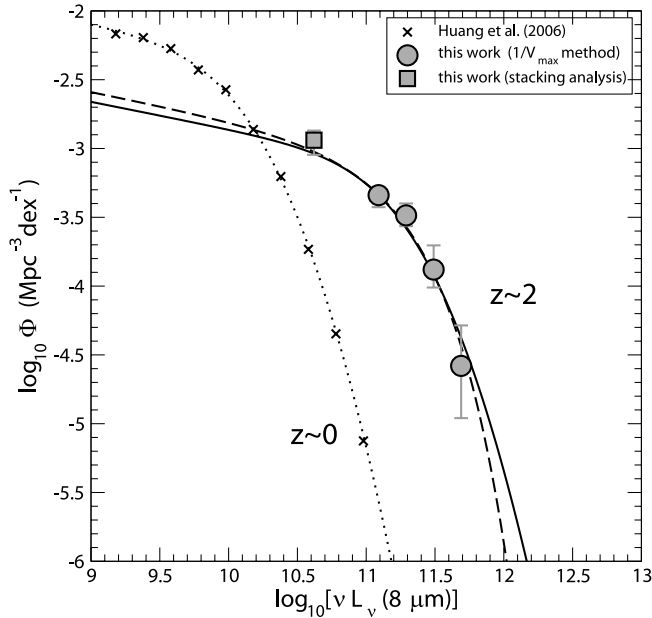
FIG. 7.—Rest-frame 8 μm LF for star-forming galaxies at $z \sim 2$ in the GOODS fields. The filled circles show the LF in the region of completeness of 8 μm luminosities, as computed with the $1/V_{\mathrm{max}}$ method. The solid and dashed lines show the 8 μm LF at $z \sim 2$ computed with the ML STY method, assuming a double exponential form as in eq. (1) and a Schechter function, respectively. The filled square is an extension of the LF at the faint end, obtained using stacking analysis (see text for details). The addition of this point a posteriori allows us to validate the extrapolated shape of the LF at the faint end. The 8 μm LF at $z \sim 0$ computed by Huang et al. (2006) has also been added for a comparison.

$\sigma = 0.36$, $\sigma = 0.20$, and a Schechter function, respectively. This is $\sim$4.0–4.3 times the corresponding luminosity density at $z \sim 0$.

5. THE REST-FRAME 8 μm LF AT REDSHIFT $z \sim 2$

5.1. The Rest-Frame 8 μm LF for Star-forming Galaxies at Redshift $z \sim 2$

The selection of 24 μm galaxies at redshift $z \sim 2$ is particularly suitable to compute the rest-frame 8 μm LF. The IR SED of star-forming galaxies is characterized by the presence of PAH emission lines from rest-frame wavelengths $\lambda = 3.3$ through 17 μm (Désert et al. 1990). In particular, one of the main features in the SED is the PAH bump around 7.7 and 8.6 μm, responsible for a positive selection effect on galaxies at $z \sim 1.9$ at 24 μm (Caputi et al. 2006c). The light associated with this bump produces a substantial fraction of the observed 24 μm output at $z \sim 2$ (the remaining part mainly being produced by AGNs). The study of the rest-frame 8 μm LF for star-forming galaxies gives direct information on the luminosity distribution of PAH emission in IR galaxies. In particular at $z \sim 2$, it should allow us to understand this PAH emission distribution when the universe was only one-fourth of its present age.

We compute the rest-frame 8 μm luminosity ($\nu L_\nu^{8\,\mu\mathrm{m}}$) of each galaxy in a similar way as for those galaxies at $0.9 < z < 1.1$. In this case, the width of the redshift bin we consider, $1.7 < z < 2.3$, implies that the observed 24 μm maps rest-frame wavelengths 7.2 μm $< \lambda_{\mathrm{rf}} < 8.9$ μm. As we have seen in § 4.1, the k-corrections are usually computed based on SED models, which have been calibrated using local IR galaxy templates and other observables. However, we showed that this can be somewhat controversial, especially in the PAH-dominated region, where different models show important discrepancies. To compute the k-corrections from 7.2–8.9 to 8 μm, we can avoid relying on

TABLE 3
The Rest-Frame 8 μm LF for Star-forming Galaxies at $z \sim 2$ Obtained with the $1/V_{\mathrm{max}}$ Method

$\log_{10}(\nu L_\nu^{8\,\mu\mathrm{m}})$	$\log_{10}\Phi(\mathrm{Mpc}^{-3}\ \mathrm{dex}^{-1})$
11.09.................................	$-3.34^{+0.06}_{-0.09}$
11.29.................................	$-3.49^{+0.09}_{-0.08}$
11.49.................................	$-3.88^{+0.18}_{-0.13}$
11.69.................................	$-4.58^{+0.29}_{-0.38}$

any IR SED model by directly using measured rest-frame IR spectra of star-forming galaxies at redshifts $z \gtrsim 1.5$, convolved with the 24 μm filter transmission function. These spectra have been obtained with the Infrared Spectrograph (IRS) for *Spitzer* (Lutz et al. 2005; Yan et al. 2005). These spectra correspond to star-forming ULIRGs that are on average brighter than those studied here. In spite of that, the k-corrections derived within the PAH region from these galaxies are expected to be applicable to our galaxies. For example, the equivalent widths of PAH lines in the Yan et al. (2005) star-forming galaxies are comparable to those of other lower luminosity ULIRGs. In general, PAH line equivalent widths appear to be quite independent of the bolometric IR luminosities of star-forming galaxies (Peeters et al. 2004; Brandl et al. 2006).

For the wavelength range considered, the k-correction factors derived from empirical spectra vary between $k = 1$ (at $\lambda_{\mathrm{rf}} = 8\ \mu$m) and $k = 1.44 \pm 0.36$ (at $\lambda_{\mathrm{rf}} = 8.9\ \mu$m). These k-corrections are in good agreement with those predicted by the Lagache et al. (2004) models. The median of the differences is $\sim$5% in the considered wavelength range (7.2–8.9 μm). Thus, the use of empirical k-corrections for our rest-frame 8 μm LF at $z \sim 2$ is consistent with the use of model-dependent k-corrections at $z = 1$.

As at redshift $z = 1$, we compute the rest-frame 8 μm LF at redshift $z \sim 2$ alternatively using the $1/V_{\mathrm{max}}$ method and the ML analysis. For the star-forming galaxy LF at this redshift, we consider the 132 star-forming galaxies with $1.7 < z < 2.3$ within our sample. The rest-frame 8 μm LF for star-forming galaxies at $z \sim 2$ computed with the two methods is shown in Figure 7 (filled circles for the $1/V_{\mathrm{max}}$ method and solid and dashed lines for the ML analysis) and Tables 3 and 4. The total comoving volume probed at these redshifts is 5.7×10^5 Mpc^{-3}.

For the $1/V_{\mathrm{max}}$ calculation, we computed the error bars taking into account Poisson statistics and the errors on photometric redshifts and k-corrections through Monte Carlo simulations. We constructed 1000 mock catalogs, each one containing 132 galaxies, as the original catalog. The redshift of each source has been allowed to randomly vary following a Gaussian distribution centered at $z_{\mathrm{center}} = z - 0.01$ and with a dispersion $\sigma_z = 0.06(1 + z)$ (see § 2.3), where z is the redshift of the source in the original catalog. The redshifts of those sources with spectroscopic determinations have been left unchanged. To include the uncertainties in the k-corrections, we computed the rest-frame 8 μm luminosity $\nu L_\nu^{8\,\mu\mathrm{m}}$ of each galaxy in the mock catalog allowing the corresponding k-correction to have a random value within the range of its error bar. Once more, we recompute the LF with the $1/V_{\mathrm{max}}$ method for each of the mock catalogs, with exactly the same procedure as for the original catalog. The distribution of the LF values in each $\nu L_\nu^{8\,\mu\mathrm{m}}$ bin determines the error bars on our original $1/V_{\mathrm{max}}$ LF.

The LF computed with the $1/V_{\mathrm{max}}$ method that is shown in Figure 7 exclusively corresponds to the region of $\nu L_\nu^{8\,\mu\mathrm{m}}$ completeness ($\nu L_\nu^{8\,\mu\mathrm{m}} \gtrsim 10^{11}\ L_\odot$). This is essential to assure that our results are not affected by incompleteness effects.

CAPUTI ET AL.

Parameter Values Characterizing the Rest-Frame 8 μm LF for Star-forming Galaxies at $z \sim 2$

Functional Form	α	σ	$\nu L_\nu^{*8\,\mu m}$ ($L_\odot$)	Φ^* (Mpc^{-3} dex^{-1})
Double exponential (eq. [1])	1.2 (fixed)	0.36 (fixed)	$(8.3^{+1.5}_{-1.1}) \times 10^{10}$	$(9.0^{+2.1}_{-1.7}) \times 10^{-4}$
Schechter (eq. [3])	1.2 (fixed)	...	$(1.62^{+0.20}_{-0.21}) \times 10^{11}$	$(9.3^{+2.1}_{-1.3}) \times 10^{-4}$

Also at these redshifts, we analyze the field-to-field variations computing the rest-frame 8 μm LF in the GOODS/CDF-S and GOODS/HDF-N separately. The results are shown in the right panel of Figure 9. We see that, in spite of the sample variance, the two LFs are still consistent within the error bars.

We perform the ML analysis for the combined fields in the same way as for galaxies at $0.9 < z < 1.1$. Once more, we assume that the double exponential form given by equation (1) with fixed slopes $\alpha = 1.2$ and $1/\sigma^2 = 1/(0.36)^2$ can be used to describe the rest-frame 8 μm LF for star-forming galaxies at $z \sim 2$. In this case, the number of galaxies is not sufficient to allow us to leave the bright-end slope as a free parameter (i.e., the ML algorithm does not converge to reasonable values). Also, the adoption of the same σ-value as at $z \sim 0$ is useful to directly compare the resulting values of L^* and Φ^* at different redshifts. Applying the STY method with a double exponential with $\sigma = 0.36$ to our star-forming galaxies at $z \sim 2$, we obtain that the value of the characteristic luminosity that maximizes the ML estimator is $L^* \equiv \nu L_\nu^{*8\,\mu m} = (8.3^{+1.5}_{-1.1}) \times 10^{10} \, L_\odot$ and the derived normalization factor is $\Phi^* = (9.0^{+2.1}_{-1.7}) \times 10^{-4}$ Mpc^{-3} dex^{-1}. The resulting curve for the ML LF at $z \sim 2$ is indicated with a solid line in Figure 7. Once more, the LF obtained with the ML analysis is in good agreement with that computed with the $1/V_{max}$ method, confirming that the double exponential form in equation (1) also provides a good description of the 8 μm LF at redshift $z \sim 2$.

As for the LF at $z = 1$, a Schechter function also appears to be an alternative suitable law to describe the rest-frame 8 μm LF for star-forming galaxies at $z \sim 2$ with the ML STY method (*dashed line in* Fig. 7).

5.2. *Testing the Faint End of the LF through Stacking Analysis*

As we mentioned in § 4.3, the faint-end slope of the IR LF is not well constrained even at $z \sim 0$, and the common procedure is to fix this slope to a given value. One could, however, put into question whether the fixed slope value we use here ($\alpha = 1.2$) is realistic to describe the faint end of the IR LF at different redshifts. In the analysis of the IR LF at redshifts $0 \lesssim z \lesssim 1.2$, Le Floc'h et al. (2005) concluded that the slope at the faint end could not be much steeper than 1.2, as otherwise the faint 24 μm number counts would be overproduced. This result has been confirmed by Zheng et al. (2006), using the stacking analysis at 24 μm of a large sample of $0.1 \lesssim z \lesssim 1$ galaxies. The stacking analysis technique allows us to gain about an order of magnitude in the IR flux detection limit (Dole et al. 2006; Zheng et al. 2006).

We do a similar stacking analysis using the $K_s < 21.5$ (Vega mag) galaxy sample presented in Caputi et al. (2006b) for the GOODS/CDF-S. We stack at 24 μm all those galaxies (except AGNs) with redshifts $1.7 < z < 2.3$ that are below the completeness limit of the $\nu L_\nu^{8\,\mu m}$ luminosities (i.e., $\nu L_\nu^{8\,\mu m} \lesssim 10^{11} \, L_\odot$ at $z \sim 2$). This includes, of course, all those $K_s < 21.5$ mag galaxies at $1.7 < z < 2.3$ in the GOODS/CDF-S that are not identified in the $S(24 \, \mu m) > 80 \, \mu$Jy catalog for the same field. We find that

the average 24 μm flux of these stacked sources is $S(24 \, \mu m) = (49.3 \pm 1.7) \, \mu$Jy, which implies an average rest-frame 8 μm luminosity $\log_{10}(\nu L_\nu^{8\,\mu m}) \approx 10.6$. To incorporate this stacking point in our differential LF expressed per dex unit, we need to estimate the flux (and thus the luminosity) range covered by the stacking sample. Also, we need to apply a correction factor that accounts for the fact that the $K_s < 21.5$ sample loses completeness in identifying 24 μm galaxies below the $S(24 \, \mu m) = 80 \, \mu$Jy limit. We perform both steps using the 24 μm number counts obtained by Papovich et al. (2004). These number counts are already corrected for incompleteness in the 24 μm detections below the flux completeness limits of the Papovich et al. (2004) samples. From the distribution of these number counts with 24 μm flux, we obtain that the average 24 μm flux of our $S(24 \, \mu m) < 80 \, \mu$Jy sample will be well reproduced if the stacked galaxies span the flux range $30 \, \mu$Jy $\lesssim S(24 \, \mu m) < 80 \, \mu$Jy. On the other hand, from the total number counts within this flux range and ignoring the effects of sample variance, we can obtain the average identification completeness produced by the $K_s < 21.5$ sample. We estimate that the $K_s < 21.5$ sample allows us to identify $\sim$79% of the 24 μm galaxies with $30 \, \mu$Jy $\lesssim S(24 \, \mu m) < 80 \, \mu$Jy. The inverse of the completeness fraction gives us the correction factor for the LF in the stacking luminosity bin. An intrinsic assumption here is that the identification completeness derived for this flux range is the same at all redshifts, so it can be applied to our $1.7 < z < 2.3$ sample. This assumption seems to be very plausible (compare the redshift distributions of the 83 μJy–limited and total 24 μm samples in Fig. 3 of Caputi et al. 2006c).

The resulting stacking point is indicated with a filled square in Figure 7. We note that we only add this point to our rest-frame 8 μm LF at $z \sim 2$ a posteriori, and it does not play any role in the ML analysis. The good agreement between the stacking analysis point and the ML curve confirms that the value fixed for the faint-end slope of the 8 μm LF is adequate, and significantly larger slopes would not reproduce the average density of faint IR galaxies.

We attempted to do a similar stacking analysis for sources at redshifts $0.9 < z < 1.1$, in order to test the faint end of the rest-frame 8 μm LF at redshift $z = 1$. However, the stacking at 24 μm of $K_s < 21.5$ ($K_s < 20.5$ mag) galaxies that are below the 8 μm luminosity completeness limit at those redshifts produces an average source with flux $S(24 \, \mu m) = 16.6$ (25.4 μJy). Unfortunately, no information on 24 μm number counts is available for or below such faint fluxes. This fact prevented us from obtaining an extension of the rest-frame 8 μm LF at $z = 1$ for faint luminosities.

5.3. *The Evolution of the Rest-Frame 8 μm LF for Star-forming Galaxies from $z \sim 0$ to $z \sim 2$*

We can now study the evolution of the rest-frame 8 μm LF from redshifts $z \sim 0$ and $z = 1$ to $z \sim 2$. Figure 8 shows the three LFs in the same plot. Different line styles in this plot correspond
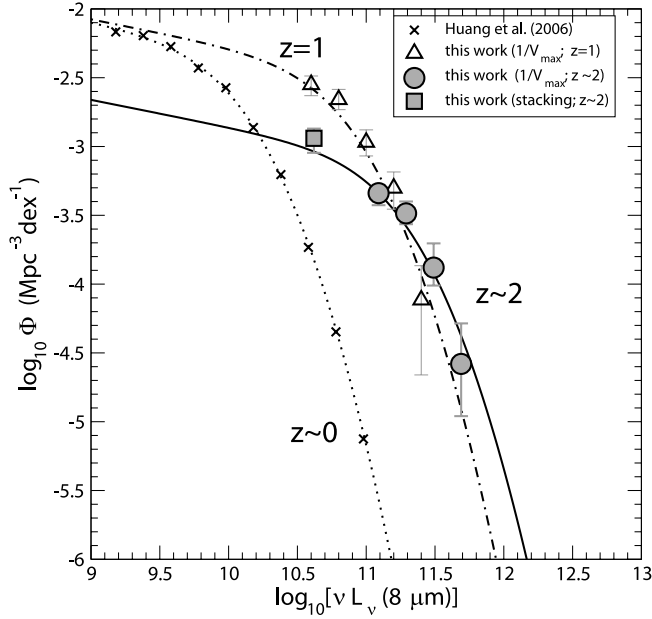
Fig. 8.—Compared rest-frame 8 μm LFs for star-forming galaxies at $z = 1$ and $\sim$2, both obtained in the GOODS fields. Symbols and lines are the same as in Fig. 7. The triangles correspond to the LF at $z = 1$, as computed with the $1/V_{\rm max}$ method. The dot-dashed line is the result of the ML analysis at the same redshift, adopting a double exponential law with $\sigma = 0.36$.

to a double exponential form with $\sigma = 0.36$. As in § 4.4, we can characterize the evolution of L^* and Φ^* with redshift. If we consider

$$L^*(z_2 \sim 2) = L^*(z_1 \sim 0)\left(\frac{1 + z_2}{1 + z_1}\right)^{\gamma_L},$$

$$\Phi^*(z_2 \sim 2) = \Phi^*(z_1 \sim 0)\left(\frac{1 + z_2}{1 + z_1}\right)^{\gamma_\delta}, \qquad (6)$$

the derived γ_L and γ_δ at strictly $z_1 = 0.2$ and $z_2 = 1.93$ are

$$\gamma_L = 3.0 \pm 0.4,$$
$$\gamma_\delta = -2.1 \pm 0.4. \qquad (7)$$

The obtained γ_L value indicates that the strong positive luminosity evolution of the rest-frame 8 μm LF continues up to redshift $z \sim 2$. In contrast, the density evolution has quite a different trend between $z \sim 0$ and $z = 1$ and between $z = 1$ and $z \sim 2$. We showed in § 4.4 that the density of galaxies with $\nu L_\nu^{8\,\mu m} \gtrsim 10^{10.5}$ $L_\odot$ dramatically increases from $z \sim 0$ and $z = 1$. Between $z = 1$ and $z \sim 2$, however, there appears to be a significant negative-density evolution. If we write

$$L^*(z_2 \sim 2) = L^*(z_1 = 1)\left(\frac{1 + z_2}{1 + z_1}\right)^{\gamma_L},$$

$$\Phi^*(z_2 \sim 2) = \Phi^*(z_1 = 1)\left(\frac{1 + z_2}{1 + z_1}\right)^{\gamma_\delta}, \qquad (8)$$

with strictly $z_1 = 1$ and $z_2 = 1.93$, we obtain

$$\gamma_L = 2.2 \pm 0.5,$$
$$\gamma_\delta = -3.9 \pm 1.0. \qquad (9)$$

A negative-density evolution at high ($z \gtrsim 1$) redshifts has also been found with some of the fittings made for the 12 μm LF by Pérez-González et al. (2005). However, these authors conclude that the result of a negative-density evolution should be taken with caution, as it could be produced by incompleteness in the faintest luminosity bins. To test this, we repeat the ML analysis of our rest-frame 8 μm LF by considering only those galaxies with $S_\nu(24\,\mu m) > 120$ μJy (which is roughly equivalent to excluding the faintest luminosity bin in the $1/V_{\rm max}$ method). In this case, the resulting normalization parameter value Φ^* implies $\gamma_\delta = -1.6 \pm 0.6$ and $\gamma_\delta = -2.7 \pm 1.3$ for the evolution between $z \sim 0$ and $z \sim 2$ and between $z = 1$ and $z \sim 2$, respectively. We conclude, then, that the negative-density evolution result is not an effect of a plausible incompleteness at the faintest luminosities.

It should be noted that all this analysis is based on the validity of the same law to describe the LF at different redshifts and the values obtained for γ_L and γ_δ depend on the adopted functional form. A more direct understanding of the evolution of the rest-frame 8 μm LF can be achieved by comparing the integrated comoving number densities of galaxies above a given luminosity

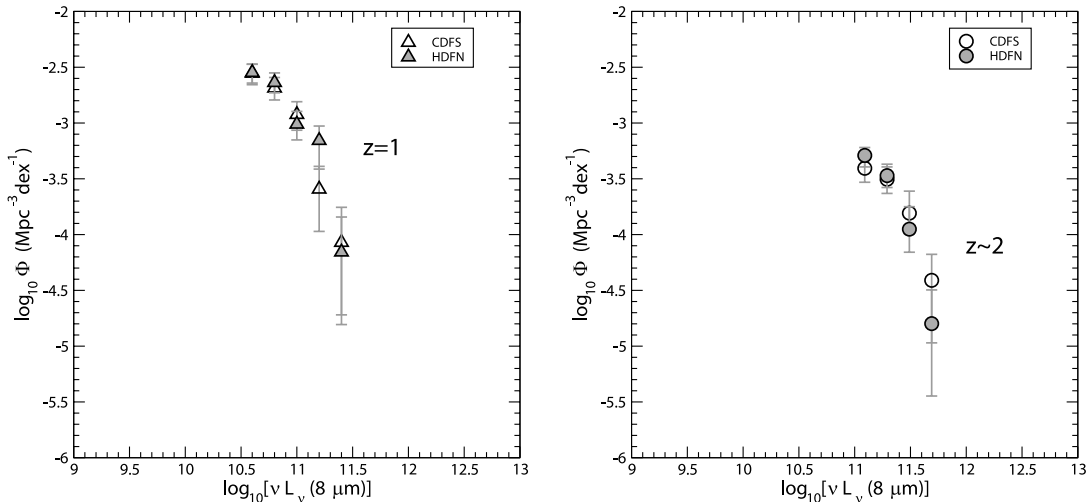Fig. 9.—Rest-frame 8 μm LF for star-forming galaxies in the GOODS/CDF-S and HDF-N separated, as computed with the $1/V_{\rm max}$ method. *Left*: $z = 1$; *right*: $z \sim 2$.

TABLE 5

Number Densities of Galaxies with Rest-Frame $\nu L_\nu^{8\,\mu m}$ above Different Luminosity Cuts at Different Redshifts

Redshift	Functional Form	$\log_{10}(\nu L_\nu^{8\,\mu m}) > 10.5$	$\log_{10}(\nu L_\nu^{8\,\mu m}) > 11.0$	$\log_{10}(\nu L_\nu^{8\,\mu m}) > 11.5$
$z \sim 0$.....................	DE ($\sigma = 0.36$)	$(4.8 \pm 0.4) \times 10^{-5}$	$(6.7 \pm 0.9) \times 10^{-7}$	$(1.4 \pm 0.3) \times 10^{-9}$
$z = 1$.....................	DE ($\sigma = 0.36$)	$(1.1 \pm 0.1) \times 10^{-3}$	$(1.8 \pm 0.3) \times 10^{-4}$	$(6.7 \pm 2.0) \times 10^{-6}$
	DE ($\sigma = 0.20$)	$(1.1 \pm 0.1) \times 10^{-3}$	$(1.7 \pm 0.3) \times 10^{-4}$	$(2.1 \pm 1.0) \times 10^{-6}$
	Schechter	$(1.1 \pm 0.1) \times 10^{-3}$	$(1.7 \pm 0.3) \times 10^{-4}$	$(2.9 \pm 1.5) \times 10^{-6}$
$z \sim 2$.....................	DE ($\sigma = 0.36$)	$(5.7 \pm 0.5) \times 10^{-4}$	$(1.7 \pm 0.2) \times 10^{-4}$	$(2.0 \pm 0.4) \times 10^{-5}$
	Schechter	$(5.8 \pm 0.4) \times 10^{-4}$	$(1.7 \pm 0.2) \times 10^{-4}$	$(1.7 \pm 0.4) \times 10^{-5}$

Notes.—These number densities have been obtained by integrating the functional form appearing in the second column and are expressed in units of Mpc^{-3}. DE stands for double exponential.

cut at different redshifts, as those we present in Table 5. If we restrict to the most luminous galaxies [$\log_{10}(\nu L_\nu^{8\,\mu m}) > 11.5$], we find that the number density increases with redshift up to $z \sim 2$. For galaxies with $\log_{10}(\nu L_\nu^{8\,\mu m}) > 11$, remarkably, the number density appears to be basically the same at redshifts $z = 1$ and $z \sim 2$. Finally, if we consider those galaxies with $\log_{10}(\nu L_\nu^{8\,\mu m}) > 10.5$, we observe a clear change of trend between $z \sim 0$ and $z = 1$ and between $z = 1$ and $z \sim 2$. While the number density of these galaxies increases by a factor >20 between $z \sim 0$ and $z = 1$, the number density at $z = 1$ decays to half its value by redshift $z \sim 2$. We note that this decrement in intermediate-luminosity galaxies is not an effect of the faint-end slope $\alpha = 1.2$ we assume for our LF. Inspection of Figure 8 shows that only a much higher α-value (which would be inconsistent with the results of stacking analysis) could make equal the number densities of $\log_{10}(\nu L_\nu^{8\,\mu m}) > 10.5$ galaxies at $z = 1$ and $z \sim 2$.

The rest-frame 8 μm luminosity density we derive at redshift $z \sim 2$ is $(7.5 \pm 0.5) \times 10^7$ [$(7.6 \pm 0.5) \times 10^7$] $L_\odot$ Mpc^{-3}, obtained by integrating the double exponential (Schechter) function from the ML analysis. This represents more than twice the 8 μm luminosity density at $z \sim 0$, but only half the corresponding luminosity density at $z = 1$.

5.4. The Total Rest-Frame 8 μm LF at Redshift $z \sim 2$

The rest-frame 8 μm LF at $z \sim 2$ we presented in § 5.1 has been calculated only taking into account the star-forming galaxies in our 24 μm–selected sample at $1.7 < z < 2.3$. In this section we recompute the rest-frame 8 μm LF at $z \sim 2$ for the GOODS fields considering all the 161 24 μm–selected star-forming galaxies and AGNs with $1.7 < z < 2.3$.

We compute the rest-frame 8 μm luminosities as explained in § 4.2. To determine the k-corrections for the AGNs in our sample, we assume that their SED follows a power law $f_\nu \propto \nu^{\alpha_{SED}}$ (with $\alpha_{SED} < 0$). For each AGN, we determine the value of α_{SED} using its IRAC 8 μm and MIPS 24 μm fluxes.

The results of the total 8 μm LF calculated with the $1/V_{max}$ method are indicated with filled diamonds in Figure 10 (see also Table 6). The error bars take into account Poisson errors and Monte Carlo simulations on the redshift and luminosity catalogs, as explained in § 5.1. Comparing this total 8 μm LF with that obtained only for star-forming galaxies (Fig. 7), we can see that AGNs mainly dominate the very bright end. This excess of very bright sources suggests that neither the double exponential form given in equation (1) nor a Schechter function is optimal to describe the bright end of the total 8 μm LF. At fainter magnitudes, however, the star-forming galaxy and total LF show no significant difference, so we can safely assume the same behavior at the faint end.

Thus, to compute the total rest-frame 8 μm LF with the STY method, we consider a combination of an exponential and a power law, as follows:

$$\Phi(L) = \begin{cases} \Phi^* \dfrac{1}{const} \left(\dfrac{L}{L^*}\right)^{1-\alpha} \\ \quad \times \exp\left[-\dfrac{1}{2\sigma^2} \log_{10}^2\left(1 + \dfrac{L}{L^*}\right)\right], & L \leq L^*, \quad (10) \\ \Phi^* \left(\dfrac{L}{L^*}\right)^{1-\beta}, & L > L^*, \end{cases}$$

where β is the slope at the bright end and the constant const = $\exp\left\{[-1/(2\sigma^2)] \log_{10}^2(2)\right\}$ guarantees continuity at $L = L^*$. The stacking analysis point (square in Fig. 10) is only added a posteriori to check the consistency of the results. In contrast to the 8 μm LF for star-forming galaxies, the bright end of the total 8 μm LF is sufficiently well constrained as to allow us to leave β as a free parameter. At the faint end, we fix $\alpha = 1.2$ and
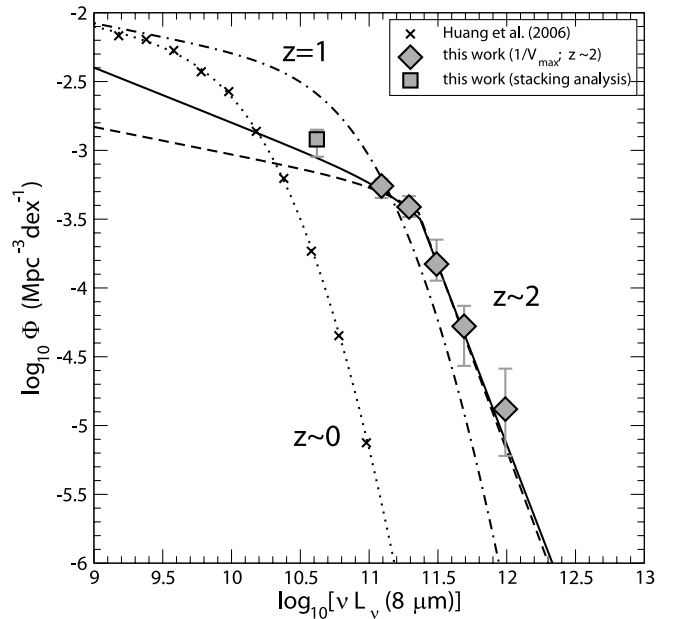

Fig. 10.—Rest-frame 8 μm LF for all the 24 μm–selected galaxies (i.e., star-forming galaxies and AGNs) at $z \sim 2$. The diamond-like symbols indicate the LF computed with the $1/V_{max}$ method. The dashed and solid lines show the LF computed with the ML analysis, assuming the functional form given in eq. (10) with $\alpha = 1.2$ and 1.4, respectively. The remaining symbols and line styles are the same as in Fig. 8.

$\log_{10}(\nu L_{\nu}^{8\,\mu m})$	$\log_{10}\Phi(\mathrm{Mpc}^{-3}\ \mathrm{dex}^{-1})$
11.09............	$-3.26^{+0.05}_{-0.09}$
11.29............	$-3.41^{+0.08}_{-0.07}$
11.49............	$-3.83^{+0.18}_{-0.12}$
11.69............	$-4.28^{+0.15}_{-0.29}$
11.99............	$-4.88^{+0.29}_{-0.34}$

$\sigma = 0.36$, as in § 5.1. The free-parameter values that yield the maximum likelihood are $\beta = 3.7^{+0.4}_{-0.3}$, $L^* \equiv \nu L_{\nu}^{*8\,\mu m} = (2.29^{+0.16}_{-0.15}) \times 10^{11}\ L_{\odot}$, and the derived normalization is $\Phi^* = (3.52^{+0.16}_{-0.13}) \times 10^{-4}\ \mathrm{Mpc}^{-3}\ \mathrm{dex}^{-1}$. The resulting ML function is plotted with a dashed line in Figure 10. We observe that while this ML LF is in very good agreement with that obtained from the $1/V_{\max}$ method, the stacking analysis point indicates that the faint end is being underproduced.

At luminosities $11.0 \lesssim \log_{10}(\nu L_{\nu}^{8\,\mu m}) \lesssim 11.4$, the $1/V_{\max}$ 8 μm LFs for star-forming and all galaxies are basically coincident. However, the slope value α that was suitable to describe the former does not seem sufficient to explain the faint end of the total LF. The explanation for this apparent contradiction is that the values of the different free parameters are coupled, and actually the definition of faint/bright ends depends on the value of L^*. In the case of the total rest-frame 8 μm LF at $z \sim 2$, the value of the characteristic luminosity L^* is significantly higher than the ML value of L^* for the star-forming galaxy LF. We recompute then the STY ML estimator for the total LF fixing the slope to a higher value $\alpha = 1.4$. The free-parameter values that yield the maximum likelihood in this case are $\beta = 3.6^{+0.5}_{-0.3}$, $L^* \equiv \nu L_{\nu}^{*8\,\mu m} = (2.34^{+0.29}_{-0.15}) \times 10^{11}\ L_{\odot}$, and the derived normalization is $\Phi^* = (3.17^{+0.15}_{-0.28}) \times 10^{-4}\ \mathrm{Mpc}^{-3}\ \mathrm{dex}^{-1}$. The ML values of β and L^* are in agreement with those corresponding to $\alpha = 1.2$, within the error bars. This indicates the robustness of the determination of the bright end and the turnover of the total 8 μm LF with our survey. The resulting ML curve for the case with $\alpha = 1.4$ is plotted with a solid line in Figure 10. This new curve appears to be consistent with the stacking analysis point.

By integrating the obtained STY LF, we can compute the 8 μm luminosity density associated with the total IR galaxy population at $1.7 < z < 2.3$. This luminosity density is $\sim(9.0 \pm 0.6) \times 10^7\ L_{\odot}\ \mathrm{Mpc}^{-3}$, i.e., ~ 2.7 times the total 8 μm luminosity density at $z \sim 0$. Comparing the total 8 μm luminosity density at $z \sim 2$ to that for only star-forming galaxies at the same redshift, $(7.5 \pm 0.5) \times 10^7\ L_{\odot}\ \mathrm{Mpc}^{-3}$, we conclude that AGNs have a minor contribution to this luminosity density even at high z ($\sim 17\%$ at $z \sim 2$).

6. THE BOLOMETRIC IR LF AT REDSHIFTS $z = 1$ AND $z \sim 2$

6.1. The Conversion from $\nu L_{\nu}^{8\,\mu m}$ to Bolometric $L_{\mathrm{bol}}^{\mathrm{IR}}$

6.1.1. A New Empirical Calibration Based on Spitzer Galaxies

In § 5 we studied the rest-frame 8 μm LF at redshift $z \sim 2$ and its evolution from $z \sim 0$. The aim of this section is to extend this study to the bolometric IR (i.e., 5 μm $\lesssim \lambda < 1000$ μm) LF. The bolometric IR luminosity of a galaxy is produced by the thermal emission of its gas content. In star-forming galaxies, the UV/optical radiation produced by young stars heats the interstellar dust and the reprocessed light is emitted in the IR. For this reason, in star-forming galaxies, the bolometric IR luminosity

allows us to obtain a direct and quite unbiased estimate of the current star formation activity.

Different methods to convert νL_{ν} luminosities into bolometric IR luminosities $L_{\mathrm{bol}}^{\mathrm{IR}}$ are common in the literature. Most of them rely on calibrations made using nearby galaxies in *IRAS* or *ISO* catalogs (e.g., Chary & Elbaz 2001; Elbaz et al. 2002; Takeuchi et al. 2005) or on the use of semiempirical SEDs (e.g., Dale & Helou 2002; Lagache et al. 2003, 2004; Dale et al. 2005). The extrapolation of these νL_{ν}-$L_{\mathrm{bol}}^{\mathrm{IR}}$ relations to high-redshift galaxies can be justified with different recent results. For example, Egami et al. (2004) showed that composite SEDs of high-z IR galaxies are well described by local templates. Also, IR galaxy models that assume such similarity in the SEDs can fit the 24, 70, and 160 μm number counts simultaneously (Lagache et al. 2004). Nevertheless, there is always some controversy on the large error bars that can be involved in the νL_{ν}-$L_{\mathrm{bol}}^{\mathrm{IR}}$ conversions applied to high redshifts. For example, Dale et al. (2005) claim that the use of 24 μm data (rest-frame 8 μm at $z \sim 2$) can produce an uncertainty of up to a factor of 5 in the derived bolometric IR luminosity of $z \sim 2$ galaxies.

To explore this issue, Bavouzet et al. (2006) studied different νL_{ν}-$L_{\mathrm{bol}}^{\mathrm{IR}}$ relations using *Spitzer* low- to intermediate-redshift galaxies. Their sample consists of 24 μm–selected galaxies with $R < 20$ (Vega mag) in three different fields, namely, the Böotes and the *Spitzer* First Look Survey fields and the extended CDF-S. The selection criterion of this sample is the detection of each galaxy in the IRAC 8 μm channel and in all three MIPS bands (i.e., at 24, 70, and 160 μm). All these galaxies have either spectroscopic or COMBO17 photometric redshifts and span the redshift range $0.0 \lesssim z \lesssim 0.6$. AGNs have been removed from their sample.

To measure the bolometric IR luminosity $L_{\mathrm{bol}}^{\mathrm{IR}}$ of each galaxy at redshift z, Bavouzet et al. (2006) used the $8-160$ μm fluxes. To integrate the corresponding empirical SED in each case, they summed up the areas below contiguous rectangles centered at rest-frame wavelengths 8 μm/(1 + z), 24 μm/(1 + z), 70 μm/(1 + z), and 160 μm/(1 + z). At longer wavelengths, they approximated the SED beyond $\lambda > [160 + (160 - 70)/2]/(1 + z) = 205$ μm/(1 + z) with a triangle of slope -4. This slope is consistent with the modified blackbody emission in the far-IR produced by big grains of dust thermalized at a temperature $T \sim 15$–20 K (Draine & Lee 1984; Conturis et al. 2001). In fact, Bavouzet et al. (2006) found that the use of any slope between -3.5 and -4.5 produced variations $<1\%$ on the computed bolometric luminosities. It is important to emphasize that the measurements of bolometric IR luminosities made by Bavouzet et al. (2006) are purely based on *Spitzer* data and are completely independent of any model template.

The resulting $L_{\mathrm{bol}}^{\mathrm{IR}}$ versus rest-frame $\nu L_{\nu}^{8\,\mu m}$ relation for the Bavouzet et al. (2006) sample is shown in Figure 11 (*plus signs*). In this work, however, we restrict the analysis only to those 93 galaxies in the Bavouzet et al. (2006) sample that have $\nu L_{\nu}^{8\,\mu m} > 10^{10}\ L_{\odot}$ and signal-to-noise ratio S/N > 3 in all the MIPS bands. The rest-frame 8 μm luminosities have been obtained applying k-corrections that do depend on different SED models (Chary & Elbaz 2001; Elbaz et al. 2002; Lagache et al. 2004). The $\nu L_{\nu}^{8\,\mu m}$-$L_{\mathrm{bol}}^{\mathrm{IR}}$ relation for these galaxies can be fitted with the following law (*dashed line in* Fig. 11):

$$L_{\mathrm{bol}}^{\mathrm{IR}} = 1.91[\nu L_{\nu}(8\ \mu m)]^{1.06}, \qquad (11)$$

with $\nu L_{\nu}(8\ \mu m)$ and $L_{\mathrm{bol}}^{\mathrm{IR}}$ expressed in units of $L_{\odot}$. The 1 σ dispersion for this relation is $\sim 55\%$. This formula is directly applicable in the redshift range $0.0 \lesssim z \lesssim 0.6$. We refer the reader to
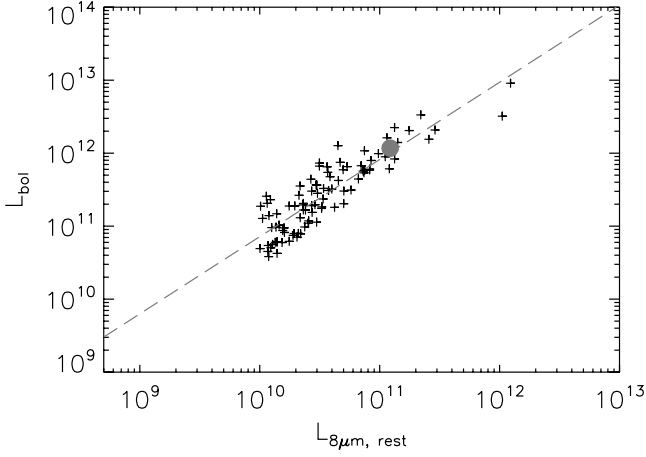
FIG. 11.—Bolometric IR vs. rest-frame 8 μm luminosity relation for galaxies with $\nu L_\nu^{8\,\mu m} > 10^{10}$ $L_\odot$ in the Bavouzet et al. (2006) sample. The plus signs indicate individual galaxies at redshifts $0.0 < z < 0.6$. The dashed line shows the best-fit relation. The filled circle shows the resulting average value of ($\nu L_\nu^{8\,\mu m}$; L_{bol}^{IR}) for a sample of galaxies at $1.3 < z < 2.3$, as obtained through stacking analysis in the GOODS/CDF-S. This point shows that the average relation between $\nu L_\nu^{8\,\mu m}$ and L_{bol}^{IR} for $1.3 < z < 2.3$ galaxies is basically the same as for galaxies at $0.0 < z < 0.6$.

the Bavouzet et al. (2006) paper for a generalized version of this formula including $\nu L_\nu^{8\,\mu m} < 10^{10}$ $L_\odot$ galaxies.

To assess whether the formula displayed in equation (11) could also be suitable to perform the $\nu L_\nu^{8\,\mu m}$-L_{bol}^{IR} conversion for higher redshift galaxies, Bavouzet et al. (2006) used the 24 μm–selected galaxy samples in the GOODS/CDF-S and HDF-N (the same samples we use in this work). Of course, the bolometric luminosity of the vast majority of $z \gtrsim 1$ galaxies cannot be empirically measured, as they are below the confusion limits of the *Spitzer* MIPS images at 70 and 160 μm. However, the average far-IR flux produced by these high-redshift sources can be recovered through stacking analysis (Dole et al. 2006).

Bavouzet et al. (2006) stacked all those 24 μm sources in the GOODS fields that lie at redshifts $1.3 < z < 2.3$, with a median redshift $z \approx 1.68$. The resulting ($\nu L_\nu^{8\,\mu m}$; L_{bol}^{IR}) value obtained with the stacking analysis is indicated with a filled circle in Figure 11. The L_{bol}^{IR} value for this point is corrected for the subestimation of the far-IR flux that is produced on high-redshift sources by using the triangle approximation method explained above. This correction is about 10%–15%. The locus occupied by the high-redshift stacked sources in the $\nu L_\nu^{8\,\mu m}$-L_{bol}^{IR} diagram strongly suggests that the relation described by equation (11) is also valid to link the 8 μm and bolometric IR luminosities of IR galaxies at $1.3 < z < 2.3$.

Thus, in this work we make use of the Bavouzet et al. (2006) relation described by equation (11) to convert the rest-frame 8 μm of our star-forming galaxies into bolometric IR luminosities. We use these resulting bolometric IR luminosities to compute the corresponding LF for star-forming galaxies at $z = 1$ and $z \sim 2$ that we present in § 6.2. As we explain in that section, the 55% dispersion found for the $\nu L_\nu^{8\,\mu m}$-L_{bol}^{IR} relation largely dominates the error budget of the bolometric IR LF.

As a final comment, we would like to discuss why the relation obtained by Bavouzet et al. (2006) predicts a significantly smaller dispersion on the values of bolometric IR luminosities L_{bol}^{IR} obtained from rest-frame 8 μm fluxes than that predicted by Dale et al. (2005). First, the Dale et al. (2005) sample includes nearby galaxies of a very different nature, and they even make separate studies of different IR regions within the same IR galaxy.

Thus, because of its selection, it is expected that the Dale et al. (2005) sample displays a larger variety of IR properties than the Bavouzet et al. (2006) sample. Furthermore, to extrapolate their conclusions to high redshifts, Dale et al. (2005) make use of the complete set of Dale & Helou (2002) models. However, the majority ($\gtrsim 75\%$) of their wide range of observed SEDs only correspond to roughly half of these models (see figures in Dale et al. 2005). The Bavouzet et al. (2006) sample has been selected with a more homogeneous criterion and includes galaxies up to intermediate ($z \approx 0.6$) redshifts. Thus, these galaxies are more likely representative of the typical galaxies selected in IR surveys. A thorough discussion of this issue is presented in the Bavouzet et al. (2006) paper.

6.1.2. *Comparison between Different $\nu L_\nu^{8\,\mu m}$-L_{bol}^{IR} Calibrations*

Several different laws to convert $\nu L_\nu^{8\,\mu m}$ into bolometric IR luminosities L_{bol}^{IR} are of common use in the literature. We analyze here how these different calibrations compare to the relation empirically derived from *Spitzer* galaxies by Bavouzet et al. (2006).

Figure 12 shows the bolometric IR L_{bol}^{IR} versus $\nu L_\nu^{8\,\mu m}$ luminosity relations (*left panel*) and the derived conversion factors $L_{bol}^{IR}/\nu L_\nu^{8\,\mu m}$ (*right panel*), both versus $\nu L_\nu^{8\,\mu m}$, as obtained using different calibrations or derived from different IR SED models. The thick solid line shows the empirical relation obtained by Bavouzet et al. (2006). The thick dashed and dotted lines correspond to the relations derived using the Lagache et al. (2004) and the Chary & Elbaz (2001) and Elbaz et al. (2002) templates, respectively. To obtain these relations, we convolve all these templates with the transmission function of the MIPS 24 μm filter. We find that the Lagache et al. (2004) model predicts a $\nu L_\nu^{8\,\mu m}$-L_{bol}^{IR} relation that is in close agreement with the Bavouzet et al. (2006) empirical calibration over all 8 μm luminosities. The Chary & Elbaz (2001) templates, on the contrary, appear to overproduce the $\nu L_\nu^{8\,\mu m}$-L_{bol}^{IR} conversion. The differences with the Bavouzet et al. (2006) calibration are only within a factor of ~ 2 for galaxies with $\nu L_\nu^{8\,\mu m} < 10^{11}$ $L_\odot$ but become dramatically larger at higher luminosities.

Previous comparisons of the νL_ν-L_{bol}^{IR} relations predicted by different models have not detected such dramatic differences (see, e.g., Le Floc'h et al. 2005). These previous comparisons analyzed longer rest-frame wavelengths, beyond the PAH-dominated region in the SEDs. The comparison we present here is made in the most critical SED region, where different models show the largest discrepancies (see also Fig. 5). From this comparison, we find that the use of the Chary & Elbaz (2001) templates to convert $\nu L_\nu^{8\,\mu m}$ into L_{bol}^{IR} luminosities leads to significantly overproduced bolometric IR luminosity values for galaxies with $\nu L_\nu^{8\,\mu m} > 10^{11}$ $L_\odot$.

In Figure 12 we also show the $\nu L_\nu^{8\,\mu m}$ to L_{bol}^{IR} derived from the Wu et al. (2005) formulae (*thin dashed lines*), which link 8 μm luminosities and star formation rates. The bolometric IR luminosities have been recovered using SFR $= 1.72 \times 10^{-10} L_{IR}$ (Kennicutt 1998). Finally, the thin dot-dashed line shows the relation used in Reddy et al. (2006b). In the latter relation, the 8 μm luminosities refer to the convolution in the wavelength range ~ 5–8.5 μm, which is somewhat different from the transmission windows of the MIPS 24 μm filter (~ 6.6–9.4 μm at $z \sim 2$) or the IRAC 8 μm filter (~ 6.5–9.5 μm; Fazio et al. 2004). Once corrected for this difference, the Reddy et al. (2006b) relation becomes closer to the Bavouzet et al. (2006) *Spitzer* calibration.

In this work we use the new *Spitzer*-based calibration given by equation (11) to convert $\nu L_\nu^{8\,\mu m}$ luminosities into bolometric IR luminosities L_{bol}^{IR}. After computing the bolometric IR LF, we analyze the contribution of LIRGs and ULIRGs to the total number
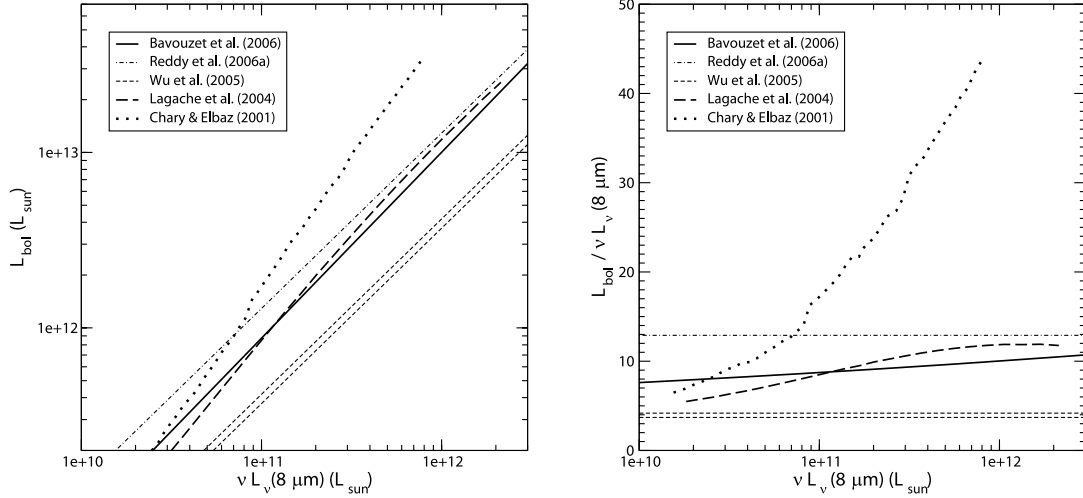
FIG. 12.—Comparison between different $L_{\rm bol}^{\rm IR}$ vs. $\nu L_{\nu}^{8\,\mu m}$ relations (*left*) and derived conversion factors vs. $\nu L_{\nu}^{8\,\mu m}$ (*right*), as obtained from different calibrations available in the literature.

and luminosity densities of IR galaxies at different redshifts. We warn the reader, however, of the implications of the differences between the $\nu L_{\nu}^{8\,\mu m}$-$L_{\rm bol}^{\rm IR}$ conversions shown in Figure 12. For example, the Chary & Elbaz (2001) conversion classifies as ULIRGs those sources with $\nu L_{\nu}^{8\,\mu m} \gtrsim 8 \times 10^{10}\ L_{\odot}$, while the Bavouzet et al. (2006) relation implies that only galaxies with $\nu L_{\nu}^{8\,\mu m} \gtrsim (1.1-1.2) \times 10^{11}\ L_{\odot}$ are ULIRGs. These differences should be kept in mind when comparing different results from the literature, where different conversion laws are used.

6.2. *The Bolometric IR LF for Star-forming Galaxies and Its Evolution to Redshift $z \sim 2$*

As we have seen in § 6.1.2, some calibrations used in the literature to convert 8 μm into bolometric IR luminosities are quite discrepant with the empirical calibration obtained from *Spitzer* galaxies. Thus, to properly compare the bolometric IR LF at different redshifts, we convert the different 8 μm LFs using the Bavouzet et al. (2006) relation shown in equation (11). The results are shown in Figure 13.

First, we transform the Huang et al. (2006) 8 μm LF at $z \sim 0$ and compute the corresponding minimum χ^2 fitting, using the functional form given in equation (1). For the bolometric IR LF at $z \sim 0$, we obtain the following best-fit parameter values: $\sigma = 0.39 \pm 0.01$, $L_{\rm IR}^* = (4.0 \pm 0.2) \times 10^{10}\ L_{\odot}$, and $\Phi^* = (5.4 \pm 0.1) \times 10^{-3}\ {\rm Mpc}^{-3}\ {\rm dex}^{-1}$. The resulting best-fit curve to the bolometric IR LF at $z \sim 0$ is shown with a dotted line in Figure 13.

The best-fit value we find for the slope at the bright end at $z \sim 0$, i.e., $\sigma = 0.39$, is very similar to the value obtained for the bright-end slope of the rest-frame 8 μm LF ($\sigma = 0.36$) at the same redshift. This similarity is due to the fact that the $\nu L_{\nu}^{8\,\mu m}$-$L_{\rm bol}^{\rm IR}$ conversion is quasi-linear.

At redshifts $z = 1$ and $z \sim 2$, we compute the bolometric IR luminosities $L_{\rm bol}^{\rm IR}$ of all our star-forming galaxies in the relevant redshift ranges by transforming their rest-frame 8 μm luminosities $\nu L_{\nu}^{8\,\mu m}$ using equation (1). We then obtain the bolometric IR LF using, alternatively, the $1/V_{\rm max}$ method and the ML STY analysis.

The upward-pointing triangles and circles in Figure 13 show the bolometric IR LF at $z = 1$ and $z \sim 2$, respectively, both computed with the $1/V_{\rm max}$ method. These LFs are only shown in the bins of completeness in $L_{\rm bol}^{\rm IR}$ luminosities, given the flux limits of our sample and the redshifts corresponding to each case. As for

the rest-frame 8 μm LF, we applied small correction factors to account for the 5%–6% identification incompleteness of the $S(24\ \mu m) > 80\ \mu$Jy galaxy sample. For both LFs, the error bars have been determined through Monte Carlo simulations, in a similar way as described in § 5.1. The mock catalogs generated in the simulations take into account the error bars in the redshift determinations, in the case of photometric redshifts. However, in the case of the bolometric luminosities, the error budget is mainly dominated by the uncertainty associated with the $\nu L_{\nu}^{8\,\mu m}$-$L_{\rm bol}^{\rm IR}$ conversion. To take into account this error, we assign to each galaxy in the mock catalogs a random bolometric IR luminosity. This random luminosity $L_{\rm bol}^{\rm IR}$ is taken from a Gaussian distribution centered at the value given by equation (11) for the corresponding galaxy and with a 55% dispersion. The recomputation of the LF with the $1/V_{\rm max}$ method on all the mock catalogs allows us to determine the error bars on the original LF calculation.
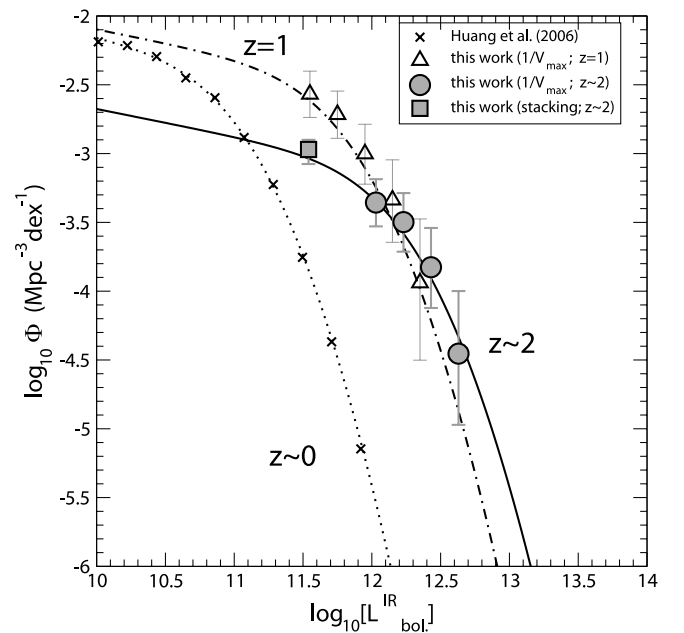

FIG. 13.—Evolution of the bolometric IR LF for star-forming galaxies from redshift $z = 0$ to $\sim$2. Symbols and line styles are the same as in Fig. 8.

TABLE 7
PARAMETER VALUES CHARACTERIZING THE BOLOMETRIC IR LF FOR STAR-FORMING GALAXIES AT $z = 1$ AND $z \sim 2$

Redshift	Functional Form	α	σ	L_{IR}^* $(L_\odot)$	Φ^* $(\mathrm{Mpc}^{-3}\,\mathrm{dex}^{-1})$
$z = 1$....................	Double exponential (eq. [1])	1.2	0.39 (fixed)	$(2.5^{+0.4}_{-0.3}) \times 10^{11}$	$(4.0^{+0.6}_{-0.5}) \times 10^{-3}$
$z \sim 2$....................	Double exponential (eq. [1])	1.2	0.39 (fixed)	$(6.3^{+1.1}_{-0.9}) \times 10^{11}$	$(9.2^{+2.2}_{-1.7}) \times 10^{-4}$

The dot-dashed and solid lines in Figure 13 indicate the bolometric IR LF at $z = 1$ and $z \sim 2$, respectively, obtained with the ML analysis. We computed the bolometric IR LF using the STY method, assuming the functional form described in equation (1). The faint- and bright-end slope values have been fixed to the $z \sim 0$ values, i.e., $\alpha = 1.2$ and $\sigma = 0.39$, respectively. At $z = 1$, we obtain that the value of the characteristic luminosity that yields the ML is $L_{\mathrm{IR}}^* = (2.5^{+0.4}_{-0.3}) \times 10^{11}\ L_\odot$. The corresponding normalization factor is $\Phi^* = (4.0^{+0.6}_{-0.5}) \times 10^{-3}\ \mathrm{Mpc}^{-3}\ \mathrm{dex}^{-1}$. At $z \sim 2$, the ML characteristic luminosity is $L_{\mathrm{IR}}^* = (6.3^{+1.1}_{-0.9}) \times 10^{11}\ L_\odot$ and the corresponding normalization factor is $\Phi^* = (9.2^{+2.2}_{-1.7}) \times 10^{-4}\ \mathrm{Mpc}^{-3}\ \mathrm{dex}^{-1}$ (see Table 7). The error bars on L_{IR}^* include the uncertainty produced by the 55% dispersion in the $\nu L_\nu^{8\,\mu\mathrm{m}}$-$L_{\mathrm{bol}}^{\mathrm{IR}}$ relation, incorporated through the mock catalogs described above. Consistently with the results obtained in §§ 4.3 and 5.1, the LFs independently calculated with the $1/V_{\mathrm{max}}$ method and the ML STY technique are in very good agreement.

Using also the $\nu L_\nu^{8\,\mu\mathrm{m}}$-$L_{\mathrm{bol}}^{\mathrm{IR}}$ relation given in equation (11), we compute the corresponding contribution of the stacked galaxies at $z \sim 2$, which are below the $L_{\mathrm{IR}}^{\mathrm{bol}}$ completeness limit of the sample, to the bolometric IR LF. Once more, the stacking analysis point appears in very good agreement with the extrapolation given by the ML analysis at the faint end of the LF.

Given the quasi-linearity of the $\nu L_\nu^{8\,\mu\mathrm{m}}$-$L_{\mathrm{bol}}^{\mathrm{IR}}$ conversion, the evolution we find for the bolometric IR LF from $z \sim 0$ to $z \sim 2$ is very similar to the evolution observed for the rest-frame 8 μm LF. For the bolometric IR LF, this implies the following:

1. The number density of galaxies with $L_{\mathrm{bol}}^{\mathrm{IR}} \gtrsim 10^{11}\ L_\odot$ substantially increases from the local universe to $z = 1$ (see Table 8). This confirms the increasing importance of the LIRG and ULIRG populations between these redshifts (see, e.g., Le Floc'h et al. 2005).

2. Surprisingly, at $z \sim 2$, the number density of star-forming ULIRGs (i.e., sources with $L_{\mathrm{bol}}^{\mathrm{IR}} > 10^{12}\ L_\odot$) is only slightly larger than at $z = 1$. This result is the combination of several factors: first, the exclusion of AGNs in this analysis produces a relatively low density of ULIRGs at $z \sim 2$, as we have seen in § 5.4 that AGNs dominate the bright end of the IR LF; second, the use of the $\nu L_\nu^{8\,\mu\mathrm{m}}$-to-$L_{\mathrm{bol}}^{\mathrm{IR}}$ conversion given in equation (11), which, in comparison to the Chary & Elbaz (2001) templates that are of common use in the literature, produces ULIRGs only from larger $\nu L_\nu^{8\,\mu\mathrm{m}}$ luminosities (see Fig. 12).

3. The number density of LIRGs (i.e., sources with $10^{11}\ L_\odot < L_{\mathrm{bol}}^{\mathrm{IR}} < 10^{12}\ L_\odot$) appears to be smaller at $z \sim 2$ than at $z = 1$. Although the limits of our survey do not allow us to directly observe LIRGs at $z \sim 2$, the ML analysis suggests this result, which is in turn validated through the stacking analysis of $z \sim 2\ K_s$-band galaxies.

Thus, the ratio between the number densities of star-forming ULIRGs and LIRGs increases from $z = 1$ to $z \sim 2$. However, within our sample and given our star-forming galaxy/AGN separation, this effect appears to be mainly produced by a decrement in the density of LIRGs by $z \sim 2$, rather than a significant increment in the density of star-forming ULIRGs. If our AGN separation criterion were excluding galaxies whose bolometric IR emission is actually dominated by star formation, then the relative importance in the number density of star-forming ULIRGs would be, of course, even larger at $z \sim 2$.

We note that the decrement we find in the number density of LIRGs between $z = 1$ and $z \sim 2$ is not influenced at all by the AGN separation criterion.

6.3. Comparison with Other Works

As we have seen in § 6.1.2, many different recipes are used in the literature to convert νL_ν into $L_{\mathrm{bol}}^{\mathrm{IR}}$ luminosities. And even different conversions made from the same wavelength (in particular, rest-frame 8 μm) may lead to nonnegligible discrepancies in the derived $L_{\mathrm{bol}}^{\mathrm{IR}}$ luminosities. In spite of these differences, it is still instructive to compare the results of different bolometric IR LF calculations.

Figure 14 compares the bolometric IR LF obtained in this work with those derived by other authors, at different redshifts. In the left panel we show the local bolometric IR LF computed from the *IRAS* revised galaxy sample (Sanders et al. 2003; *diamonds*) and the bolometric IR LF derived in this work from the Huang et al. (2006) rest-frame 8 μm LF at $z \sim 0.2$. The difference between the two is mainly due to a real evolution between $z = 0$ and $z \sim 0.2$. In the same panel, we also compare our bolometric IR LF at $z = 1$ with that obtained by Le Floc'h et al. (2005) at $z = 0.9$. We observe that both LFs are in good agreement, taking into account the error bars and the evolution expected between these redshifts (cf. Le Floc'h et al. 2005).

In the right panel of Figure 14 we show our bolometric IR LF at redshift $z \sim 2$, compared to that derived from Pérez-González

TABLE 8
NUMBER DENSITIES OF STAR-FORMING LIRGS AND ULIRGS AT DIFFERENT REDSHIFTS

Redshift	Functional Form	$\log_{10} L_{\mathrm{bol}}^{\mathrm{IR}} > 11$	LIRG	ULIRG
$z \sim 0$....................	DE ($\sigma = 0.39$)	$(4.1 \pm 0.3) \times 10^{-4}$	$(4.1 \pm 0.3) \times 10^{-4}$	$(3.9 \pm 0.7) \times 10^{-7}$
$z = 1$....................	DE ($\sigma = 0.39$)	$(2.6 \pm 0.1) \times 10^{-3}$	$(2.5 \pm 0.2) \times 10^{-3}$	$(1.2 \pm 0.2) \times 10^{-4}$
$z \sim 2$....................	DE ($\sigma = 0.39$)	$(1.1 \pm 0.1) \times 10^{-3}$	$(9.5 \pm 1.5) \times 10^{-4}$	$(1.5 \pm 0.2) \times 10^{-4}$

NOTES.—These number densities have been obtained by integrating the functional form appearing in the second column and are expressed in units of Mpc^{-3}. DE stands for double exponential.
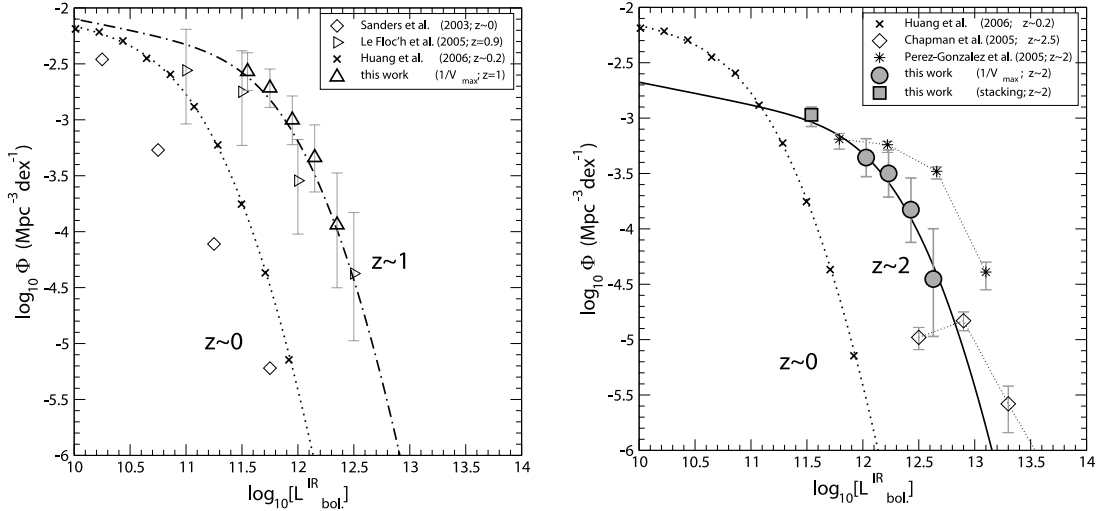
Fig. 14.—Bolometric IR LF obtained in this work compared to the determinations of other authors at similar redshifts: $z \sim 1$ (*left*) and $z \sim 2$ (*right*).

et al. (2005) at a similar redshift and that computed from radio-detected submillimeter galaxies at $z \sim 2.5$ (Chapman et al. 2005).

The bolometric IR LF derived from Pérez-González et al. (2005; *asterisks in* Fig. 14) has been obtained by converting their rest-frame 12 μm LF at $z \sim 2$, using the same recipe adopted by these authors to obtain bolometric IR luminosity densities (see eq. [1] in their paper). This conversion corresponds to the Chary & Elbaz (2001) $\nu L_\nu^{12\ \mu m}$-L_{bol}^{IR} formula. Our bolometric IR LF at $z \sim 2$ is in agreement, within the error bars, with that derived from Pérez-González et al. (2005) at luminosities $L_{bol}^{IR} \lesssim 10^{12.5}\ L_\odot$. At brighter luminosities, however, the two LFs present significant discrepancies. The differences between the two are produced by two factors: (1) the AGN exclusion: Pérez-González et al. (2005) only exclude the most extreme cases of AGNs, while here we adopt a more extensive separation criterion; (2) the different νL_ν-L_{bol}^{IR} conversions: as we have seen in § 6.1.2, the most drastic differences between the empirical *Spitzer*-based conversion we use in this work and that derived from the Chary & Elbaz (2001) and Elbaz et al. (2002) templates occur at luminosities $L_{bol}^{IR} \gtrsim 10^{12}\ L_\odot$. This comparison illustrates the impact of using different νL_ν-L_{bol}^{IR} relations, especially at high redshifts, where the most luminous IR galaxies are dominant.

The bolometric IR luminosities derived from radio-detected submillimeter galaxies only can trace the very bright end of the bolometric IR LF. The diamonds in the right panel of Figure 14 correspond to the submillimeter-derived bolometric IR LF at $z \sim 2.5$, as obtained by Chapman et al. (2005). This LF does not exclude AGNs and quickly loses completeness at $L_{bol}^{IR} \lesssim 10^{13}\ L_\odot$. Taking into account these facts and the differences in redshift, we find that the Chapman et al. (2005) bolometric IR LF at $z \sim 2.5$ is consistent with our LF based on 24 μm–selected galaxies at $z \sim 2$.

6.4. *The Evolution of the Bolometric IR Luminosity Density*

One of the final aims of computing the bolometric IR LF is to obtain an estimate of the IR luminosity density (in our case associated with star-forming galaxies) at a given look-back time. Previous works agree in a strong evolution of the IR luminosity density from the local universe up to redshift $z \sim 1$ (e.g., Flores et al. 1999; Gispert et al. 2000; Pozzi et al. 2004; Le Floc'h et al. 2005). At higher redshifts, the situation is less clear, as only recently are IR facilities allowing us to put constraints on the IR universe at $z \gtrsim 1$.

Given the discrepancies existing between different recipes to obtain bolometric IR luminosities (see § 6.1.2), we need to use the bolometric IR LF obtained with the same conversion at different redshifts, in order to properly compute the evolution of the IR luminosity density.

Figure 15 shows the evolution of the comoving IR luminosity density as a function of redshift. Our determinations of the IR luminosity density at $z = 1$ and $z \sim 2$ (strictly $z = 1.93$) are indicated with a filled upward-pointing triangle and circle, respectively: $\Omega_{IR}(z = 1) = (1.2 \pm 0.2) \times 10^9\ L_\odot\ \mathrm{Mpc}^{-3}$ and
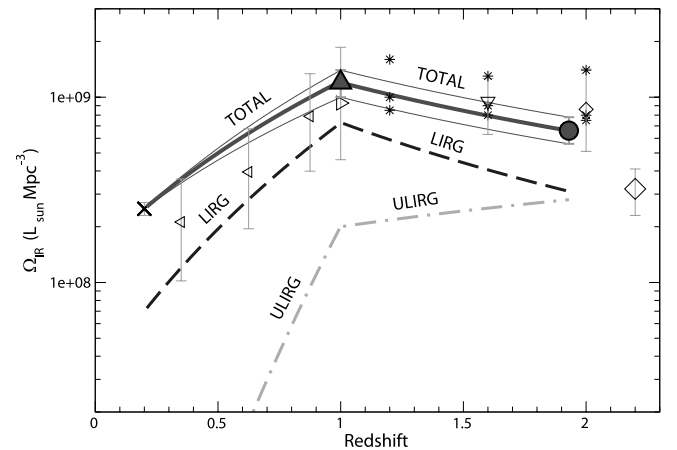

Fig. 15.—Evolution of the comoving bolometric IR luminosity density with redshift. The filled upward-pointing triangle and circle at redshifts $z = 1$ and 1.93 indicate the estimations of the respective bolometric IR luminosity density obtained in this work: $\Omega_{IR} = (1.2 \pm 0.2) \times 10^9$ and $(6.6^{+1.2}_{-1.0}) \times 10^8\ L_\odot\ \mathrm{Mpc}^{-3}$. The density at $z = 0.2$ has been obtained from the bolometric IR LF derived from the 8 μm LF by Huang et al. (2006). The thick solid line corresponds to an interpolation between these redshifts, assuming a $[(1 + z_2)/(1 + z_1)]^x$ evolution. The thin solid lines indicate error bars on this evolution. Dashed and dot-dashed lines show the contributions of LIRGs and ULIRGs, respectively, at different redshifts. Other symbols refer to IR luminosity densities taken from the literature and based on different data sets: *ISO* mid-IR (Flores et al. 1999; *left-pointing triangles*), *Spitzer* mid-IR (Le Floc'h et al. 2005; Pérez-González et al. 2005; *right-pointing triangle and asterisks, respectively*), submillimeter (Barger et al. 2000; Chapman et al. 2005; *small and large diamonds, respectively*), and radio (Haarsma et al. 2000; *downward-pointing triangle*). Some of these IR luminosity densities have been obtained from the star-formation rate densities compiled by Hopkins (2004) and converted with the Kennicutt (1998) formula SFR = $1.72 \times 10^{-10}L_{IR}$. [*See the electronic edition of the Journal for a color version of this figure.*]

$\Omega_{IR}(z \sim 2) = (6.6^{+1.2}_{-1.1}) \times 10^8 \ L_\odot \ \mathrm{Mpc}^{-3}$. We obtain the values of these luminosity densities by integrating our respective bolometric IR LFs obtained with the ML likelihood analysis, weighted with the luminosity values. The error bars are determined by the extreme cases of LFs produced by the error bars on L^*_{IR}.

The cross in Figure 15 represents the bolometric IR luminosity density at $z \sim 0$ (strictly $z = 0.2$), as obtained from the bolometric IR LF derived from the Huang et al. (2006) 8 μm LF: $\Omega_{IR}(z \sim 0) = (2.5 \pm 0.2) \times 10^8 \ L_\odot \ \mathrm{Mpc}^{-3}$.

The thick solid line in Figure 15 interpolates the evolution of the total bolometric IR luminosity density between redshifts $z_1 \sim 0$ to $z_2 = 1$ and $z_1 = 1$ to $z_2 \sim 2$, assuming that this evolution follows a $[(1+z_2)/(1+z_1)]^x$ law. Between redshifts $z \sim 0$ and $z = 1$, we find that the total bolometric IR luminosity density increases as $[(1+z_2)/(1+z_1)]^{3.1 \pm 0.3}$ (where $z_1 = 0.2$ and $z_2 = 1.0$). This evolution is somewhat slower than that obtained by Le Floc'h et al. (2005), who found $[(1+z_2)/(1+z_1)]^{3.9}$ between $z_1 = 0$ and $z_2 = 1$. The bolometric IR luminosity density at $z = 1$ determined by Le Floc'h et al. (2005; *right-pointing triangle in* Fig. 15) is actually very close to the value we determine here. The difference appears to be mainly produced in the IR luminosity density at low redshifts: there has been a significant evolution of the IR LF between redshifts $z = 0$ and $z \sim 0.2$.

Other symbols in Figure 15 refer to different bolometric IR luminosity density estimations derived from different data sets: radio (Haarsma et al. 2000; *downward-pointing triangle*), submillimeter (Barger et al. 2000; *diamond*), and the different fits made on mid-IR data by Pérez-González et al. (2005; *asterisks*). Our determinations of the IR luminosity densities are in good agreement with most of these previous works within the error bars. Our results exclude, however, the highest of the three estimations made by Pérez-González et al. (2005) at $z \gtrsim 1$.

Finally, in Figure 15 we show the relative contributions of the LIRG and ULIRG populations to the total IR luminosity density, as a function of redshift. At $z \sim 0$, 28^{+11}_{-20} % of the bolometric IR luminosity density is contained in LIRGs and <1% in ULIRGs. At $z = 1$, we find that LIRGs and ULIRGs contribute 61^{+4}_{-7}% and 16^{+11}_{-12} %, respectively, to the total IR luminosity density, in agreement with Le Floc'h et al. (2005) within the error bars. By $z \sim 2$, the contribution of LIRGs and ULIRGs becomes 47^{+13}_{-11} % and 42^{+15}_{-22} % of the total budget, respectively.

Using the Kennicutt formula SFR $= 1.72 \times 10^{-10} L_{IR}$, we can convert the bolometric IR luminosity densities into star formation rate densities at different redshifts. At $z = 1$ and $z \sim 2$, respectively, $\Omega_{IR} = (1.2 \pm 0.2) \times 10^9$ and $(6.6^{+1.2}_{-1.0}) \times 10^8 \ L_\odot \ \mathrm{Mpc}^{-3}$ translate into star formation rate densities $\delta_{SFR} \approx 0.20 \pm 0.03$ and $0.11 \pm 0.02 \ M_\odot \ \mathrm{yr}^{-1} \ \mathrm{Mpc}^{-3}$ (assuming a Salpeter initial mass function over stellar masses $M = 0.1$–$100 \ M_\odot$). In § 7 we make use of our current knowledge on stellar mass density evolution to discuss why these derived star formation rate densities could not be much higher than this value at redshifts $1 \lesssim z \lesssim 3$.

7. DISCUSSION

If the IR LF for star-forming galaxies follows a unique law from the local universe to high redshifts, then the results of our LF determination will imply that there is a negative evolution in the overall number density of IR star-forming galaxies between $z \sim 0$ and ~ 2. We showed here the validity of a universal law to describe the IR LF at intermediate and bright luminosites, at different redshifts. Of course, one could argue that the faint end of this LF is not sufficiently well constrained as to determine the number density of low-luminosity objects. Although a direct probe of the faint end of the IR LF will require the capabilities of next-

generation telescopes such as the *James Webb Space Telescope* (*JWST*), the stacking analysis of galaxies below the limits of our 24 μm survey appears to support our conclusion. The result of stacking analysis suggests that the faint-end slope of the IR LF at $z \sim 2$ cannot be much higher than the value we considered here (and those usually considered in the literature at different redshifts).

In fact, an analogous situation is observed at other wavelengths. For example, Caputi et al. (2006b) determined the evolution of the rest-frame K_s-band LF from $z = 0$ to $z \sim 2.5$. The depth of their survey ($K_s < 21.5$ Vega mag) allowed them to properly constrain this LF down to more than a magnitude below the turnover M^* at $z = 2$. These authors found that a Schechter function with the same fixed slope is suitable to describe the K_s-band LF from the local universe to high redshifts, within the limits of their survey. In this case, the ML analysis (which is in good agreement with the LF computed with the $1/V_{max}$ method) also indicates that there is a negative-density evolution of this LF with increasing redshift.

The similarities between the evolutions of the K_s-band and 8 μm LFs should not come as a surprise. The bright end of the mid-IR LF at $z \sim 2$ is mostly populated by massive $M \gtrsim 10^{11} \ M_\odot$ galaxies (Caputi et al. 2006c). At redshift $z \sim 1$, the mid-IR LF is dominated by LIRGs, the majority of which are characterized by intermediate ($\sim 10^{10}$–$10^{11} \ M_\odot$) stellar masses (Hammer et al. 2005; Caputi et al. 2006c). Thus, the evolution in the number density of mid-IR galaxies above a given luminosity cut is related to the global evolution of galaxies above a given mass cut.

It should be clear that the aim of this discussion is to show how the results we find in this work are perfectly consistent with other observational evidence of galaxy evolution. This does not exclude, however, that the ultimate conclusion on the faint ends of the K_s and IR LF will only be achieved in the light of future extremely deep surveys.

As we mentioned in § 6.4, the IR luminosity density associated with star-forming galaxies at $z \sim 2$ implies a star formation rate density $0.11 \pm 0.02 \ M_\odot \ \mathrm{yr}^{-1} \ \mathrm{Mpc}^{-3}$ (Kennicutt 1998). Let us assume that this has been the average star formation rate density between redshifts $z = 1$ and 3. In our assumed cosmology, the elapsed time between these redshifts is ~ 3.6 Gyr. The stellar mass density formed during this period of time would be nearly $(4.0 \pm 0.7) \times 10^8 \ M_\odot \ \mathrm{Mpc}^{-3}$. If we consider that the fraction of material recycled through stellar winds and supernovae could be roughly 50%, then the resulting mass density locked in stars would grow by $\sim (2.0 \pm 0.4) \times 10^8 \ M_\odot \ \mathrm{Mpc}^{-3}$ between $z = 3$ and 1. This is actually the growth of the stellar mass density that has been measured from different near-IR surveys at these redshifts (see Caputi et al. 2006b and references therein). This result also shows that, unless the recycled fraction of material into the interstellar medium is much larger than 50% between redshifts $z = 1$ and 3, then the average star formation rate density along this period cannot very much exceed the value we find in this work, $\delta_{SFR} \approx 0.11 \pm 0.02 \ M_\odot \ \mathrm{yr}^{-1} \ \mathrm{Mpc}^{-3}$ at $z \sim 2$. Much higher star formation rate densities only could be explained if a high fraction of the new formed stars were very massive, in which case they would basically not contribute to the final stellar mass of the host galaxies.

Considering a star formation rate density $\delta_{SFR} = 0.11 \pm 0.02 \ M_\odot \ \mathrm{yr}^{-1} \ \mathrm{Mpc}^{-3}$ strictly in the redshift range $1.7 < z < 2.3$ and assuming again a recycled fraction of 50%, we derive that the total stellar mass density produced in this redshift interval is $(1.8 \pm 0.3) \times 10^7 \ M_\odot \ \mathrm{Mpc}^{-3}$. This is nearly 4% of the total stellar mass density assembled at $z = 0$ [i.e., $(4.9 \pm 0.1) \times 10^8 \ M_\odot \ \mathrm{Mpc}^{-3}$, as obtained by integrating the local stellar mass

function of, e.g., Cole et al. 2001]. In the redshift interval $0.9 < z < 1.1$, our measured star formation rate density is $\delta_{SFR} = 0.20 \pm 0.03 \, M_\odot \, \text{yr}^{-1} \, \text{Mpc}^{-3}$. With a recycled fraction of 50%, this implies a growth in stellar mass density of $(8.0 \pm 1.2) \times 10^7 \, M_\odot \, \text{Mpc}^{-3}$. Thus, more than 15% of the present-day stellar mass density is being created in IR galaxies during the time elapsed between redshifts $z = 0.9$ and 1.1 (i.e., ~ 0.8 Gyr).

We found in this work that the number densities of ULIRGs associated with star formation are very similar at redshifts $z = 1$ and ~ 2. This suggests that the physical mechanism responsible for galaxies to enter a star-forming ULIRG phase is similarly efficient at these two redshifts. This result imposes strong constraints on IR galaxy synthesis models. The origin of the ULIRG phase is usually associated with advanced gas-rich mergers (Sanders & Mirabel 1996). Thus, this phenomenon had to be comparably common for the production of powerful star-forming systems at redshifts $z = 1$ and 2.

8. SUMMARY AND CONCLUSIONS

In this work we have presented the IR LF of 24 μm–selected *Spitzer* galaxies at redshifts $z = 1$ and ~ 2 in the GOODS fields. At $z \sim 2$, we separately studied the LF for star-forming galaxies only and the total 8 μm LF for star-forming galaxies and AGNs. We then used a new calibration based on *Spitzer* star-forming galaxies to convert the rest-frame 8 μm into bolometric IR luminosities of the star-forming galaxies in our sample. This allowed us to compute the bolometric IR LF and obtain an estimate of the IR luminosity densities at $z = 1$ and ~ 2.

We found that the rest-frame 8 μm LF for star-forming galaxies at $z = 1$ and ~ 2 is well described by a double exponential law that has evolved from $z \sim 0$. Between $z \sim 0$ and $z = 1$, there is a strong luminosity evolution and the number density of $\log_{10}(\nu L_\nu^{8 \, \mu m}) > 10.5$ increases by a factor >20. The characteristic luminosity L^* of the rest-frame 8 μm LF continues increasing up to redshift $z \sim 2$, but, at this redshift, the number density of $\log_{10}(\nu L_\nu^{8 \, \mu m}) > 10.5$ galaxies is smaller than the density at $z = 1$. This certainly does not mean that the contribution of IR galaxies has been less important at high redshifts. The rest-frame 8 μm luminosity density at $z \sim 2$ is still ~ 2.3 times larger than the corresponding luminosity density at $z \sim 0$, but only half the value at $z = 1$.

At $z \sim 2$, the inclusion of AGNs mainly affects the bright end of the IR LF. The bright end of the total rest-frame 8 μm LF for star-forming galaxies and AGNs is correctly reproduced by a power law that accounts for the excess of bright sources. AGNs only produce $\sim 17\%$ of the total rest-frame 8 μm luminosity density at $z \sim 2$.

The quasi-linear relation between rest-frame 8 μm and bolometric IR luminosities for star-forming galaxies produces that the bolometric IR LF is well described by a similar law as the rest-frame 8 μm LF at the same redshift. The characteristic luminosity L_{IR}^* of the bolometric IR LF for star-forming galaxies at $z \sim 2$ is close to $\sim 10^{12} \, L_\odot$, i.e., the limiting luminosity between the LIRGs and ULIRGs. As the luminosity density is mainly governed by the turnover of the LF, the value of L_{IR}^* results in roughly similar contributions of LIRGs and ULIRGs to the IR luminosity density. These two populations altogether account for $\sim 90\%$ of the total IR luminosity density associated with star formation at $z \sim 2$.

Finally, we discussed the possibility that the total IR luminosity and corresponding star formation rate density estimated in this work could have been significantly different at any redshift between $z = 1$ and 3. Constraints from near-IR surveys suggest that the stellar mass density built up by galaxies at this epoch would be in contradiction with average star formation rate densities much larger than our estimated value (unless a much higher proportion of very massive stars were created in the past). Our results appear, then, to be consistent with this other observational evidence of galaxy evolution.

REFERENCES

Alexander, D., et al. 2003, AJ, 126, 539
Babbedge, T. S. R., et al. 2006, MNRAS, 370, 1159
Barger, E. J., Cowie, L. L., & Richards, E. A. 2000, AJ, 119, 2092
Barmby, P., et al. 2006, ApJ, 642, 126
Bavouzet, N., et al. 2006, A&A, submitted
Bertin, E., & Arnouts, S. 1996, A&AS, 117, 393
Bolzonella, M., Miralles, J.-M., & Pelló, R. 2000, A&A, 363, 476
Brandl, B. R., et al. 2006, ApJ, 653, 1129
Bruzual, A. G., & Charlot, S. 1993, ApJ, 405, 538
Calzetti, D., Armus, L., Bohlin, R. C., Kinney, A. L., Koornneef, J., & Storchi-Bergmann, T. 2000, ApJ, 533, 682
Calzetti, D., et al. 2005, ApJ, 633, 871
Capak, P., et al. 2004, AJ, 127, 180
Caputi, K. I., Dole, H., Lagache, G., McLure, R. J., Dunlop, J. S., Puget, J.-L., Le Floc'h, E., & Pérez-González, P. G. 2006a, A&A, 454, 143
Caputi, K. I., McLure, R. J., Dunlop, J. S., Cirasuolo, M., & Schael, A. M. 2006b, MNRAS, 366, 609
Caputi, K. I., et al. 2006c, ApJ, 637, 727
Chapman, S. C., Blain, A. W., Smail, I., & Ivison, R. J. 2005, ApJ, 622, 772
Chary, R., & Elbaz, D. 2001, ApJ, 556, 562

Chary, R., et al. 2007, ApJ, submitted
Cohen, J. G., Cowie, L. L., Hogg, D. W., Songaila, A., Blandford, R., Hu, E. M., & Shopbell, P. 1996, ApJ, 471, L5
Cole, S., et al. 2001, MNRAS, 326, 255
Contursi, A., Boselli, A., Gavazzi, G., Bertagna, E., Tuffs, R., & Lequeux, J. 2001, A&A, 365, 11
Dale, D. A., & Helou, G. 2002, ApJ, 576, 159
Dale, D. A., Helou, G., Contursi, A., Silbermann, N. A., & Kolhatkar, S. 2001, ApJ, 549, 215
Dale, D. A., et al. 2005, ApJ, 633, 857
Désert, F.-X., Boulanger, F., & Puget, J.-L. 1990, A&A, 237, 215
Dole, H., et al. 2004, ApJS, 154, 93
———. 2006, A&A, 451, 417
Draine, B. T., & Lee, H. M. 1984, ApJ, 285, 89
Egami, E., et al. 2004, ApJS, 154, 130
Elbaz, D., et al. 2002, A&A, 384, 848
Fazio, G. G., et al. 2004, ApJS, 154, 10
Flores, H., et al. 1999, ApJ, 517, 148
Förster-Schreiber, N. M., Roussel, H., Sauvage, M., & Charmandaris, V. 2004, A&A, 419, 501

Galliano, F., Madden, S. C., Jones, A. P., Wilson, C. D., & Bernard, J.-P. 2005, A&A, 434, 867

Giacconi, R., et al. 2002, ApJS, 139, 369

Giavalisco, M., et al. 2004, ApJ, 600, L93

Gispert, R., Lagache, G., & Puget, J.-L. 2000, A&A, 360, 1

Greve, T. R., Ivison, R. J., Bertoldi, F., Stevens, J. A., Dunlop, J. S., Lutz, D., & Carilli, C. L. 2004, MNRAS, 354, 779

Haarsma, D. B., Partridge, R. B., Windhorst, R. A., & Richards, E. A. 2000, ApJ, 544, 641

Hammer, F., Flores, H., Elbaz, D., Zheng, X. Z., Liang, Y. C., & Cesarsky, C. 2005, A&A, 430, 115

Hopkins, A. M. 2004, ApJ, 615, 209

Hornschemeier, A. E., et al. 2001, ApJ, 554, 742

———. 2003, AJ, 126, 575

Huang, J., et al. 2006, ApJ, submitted

Ilbert, O., et al. 2005, A&A, 439, 863

Kennicutt, R. C., Jr. 1998, ApJ, 498, 541

Lacy, M., et al. 2004, ApJS, 154, 166

Lagache, G., Dole, H., & Puget, J.-L. 2003, MNRAS, 338, 555

Lagache, G., et al. 2004, ApJS, 154, 112

Le Borgne, D., & Rocca-Volmerange, B. 2002, A&A, 386, 446

Le Fèvre, O., et al. 2004, A&A, 428, 1043

Le Floc'h, E., et al. 2004, ApJS, 154, 170

———. 2005, ApJ, 632, 169

———. 2007, ApJ, in press

Lonsdale, C., et al. 2004, ApJS, 154, 54

Lutz, D., et al. 2005, ApJ, 625, L83

Papovich, C., et al. 2004, ApJS, 154, 70

Peeters, E., Spoon, H. W. W., & Tielens, A. G. G. M. 2004, ApJ, 613, 986

Pérez-González, P. G., et al. 2005, ApJ, 630, 82

Pozzi, F., et al. 2004, ApJ, 609, 122

Reddy, N., Steidel, C. C., Erb, D. K., Shapley, A. E., & Pettini, M. 2006a, ApJ, 653, 1004

Reddy, N., Steidel, C. C., Fadda, D., Yan, L., Pettini, M., Shapley, A. E., Erb, D. K., & Adelberger, K. L. 2006b, ApJ, 644, 792

Rieke, G. H., et al. 2004, ApJS, 154, 25

Roussel, H., Sauvage, M., Vigroux, L., & Bosma, A. 2001, A&A, 372, 427

Sandage, A., Tammann, G. A., & Yahil, A. 1979, ApJ, 232, 352

Sanders, D. B., Mazzarella, J. M., Kim, D.-C., Surace, J. A., & Soifer, B. T. 2003, AJ, 126, 1607

Sanders, D. B., & Mirabel, I. F. 1996, ARA&A, 34, 749

Sanders, D. B., et al. 2007, ApJS, in press

Saunders, W., et al. 1990, MNRAS, 242, 318

Schechter, P. 1976, ApJ, 203, 297

Schmidt, M. 1968, ApJ, 151, 393

Scott, S. E., et al. 2002, MNRAS, 331, 817

Serjeant, S., et al. 2004, MNRAS, 355, 813

Stern, D., et al. 2005, ApJ, 631, 163

Takeuchi, T. T., Buat, V., Iglesias-Páramo, J., Boselli, A., & Burgarella, D. 2005, A&A, 432, 423

Takeuchi, T. T., Ishii, T. T., Dole, H., Dennefeld, M., Lagache, G., & Puget, J.-L. 2006, A&A, 448, 525

Takeuchi, T. T., Yoshikawa, K., & Ishii, T. T. 2003, ApJ, 587, L89

Vanzella, E., et al. 2005, A&A, 434, 53

———. 2006, A&A, 454, 423

Webb, T. M., et al. 2003, ApJ, 587, 41

Werner, M. W., et al. 2004, ApJS, 154, 1

Wirth, G. D., et al. 2004, AJ, 127, 3121

Wolf, C., et al. 2004, A&A, 421, 913

Wu, H., et al. 2005, ApJ, 632, L79

Xu, C. 2000, ApJ, 541, 134

Yan, L., et al. 2004, ApJS, 154, 60

———. 2005, ApJ, 628, 604

Zheng, X. Z., et al. 2006, ApJ, 640, 784

Zucca, E., Pozzetti, L., & Zamorani, G. 1994, MNRAS, 269, 953